11-20-2008

# A J/\Psi Polarization Measurement with the Phenix Muon Arms in Proton+Proton Collisions at Center of Mass Energy of 200 GEV at RHIC

Hai Qu

# A $J/\Psi$ POLARIZATION MEASUREMENT WITH THE PHENIX MUON ARMS IN PROTON+PROTON COLLISIONS AT CENTER OF MASS ENERGY OF 200 GEV AT RHIC

by

HAI QU

Under the Direction of Xiaochun He

ABSTRACT

A measurement of $J/\psi$ polarization has been performed for 200 GeV proton+proton collisions with the PHENIX Muon Arms at RHIC. The results from the current data show no polarization within the PHENIX acceptance range. The results are consistent with the current model predictions and other experimental measurements.

INDEX WORDS: RHIC, PHENIX, Proton+proton collisions, $J/\psi$, Polarization
200 GeV

# A $J/\Psi$ POLARIZATION MEASUREMENT WITH THE PHENIX MUON ARMS IN PROTON+PROTON COLLISIONS AT CENTER OF MASS ENERGY OF 200 GEV AT RHIC

by

HAI QU

A Dissertation Submitted in Partial Fullfilment of the Requirements for the Degree of

Doctor of Philosophy

in the College of Arts and Sciences

Georgia State University

2008

# A $J/\Psi$ POLARIZATION MEASUREMENT WITH THE PHENIX MUON ARMS IN PROTON+PROTON COLLISIONS AT CENTER OF MASS ENERGY OF 200 GEV AT RHIC

by

HAI QU

Committee Chair: Dr. Xiaochun He

Committee: Dr. Steven Manson

Dr. William Nelson

Dr. Brian Thoms

Dr. Douglas Gies

Electronic Version Approved:

Office of Graduate Studies
College of Arts and Sciences
Georgia State University
December 2008

To my parents, Youdi Zhang and Yishen Qu

## Acknowledgments

I would like to take this opportunity to thank many people who helped to make this work possible. These include my advisors, my colleagues, my friends, and my family. Although the list of individuals I wish to thank extends beyond the limits of this format, I would like to thank the following people for their dedication, encouragement, and support:

I would first like to express profound gratitude to my supervisor, Dr. Xiaochun He, for his invaluable support, encouragement, supervision, and useful suggestions throughout this research work. He has led me in this field and taught me so many things from which I will continue to benefit in my future career. Not only has he given me guidance, but also he has been working with me to solve problems. I have greatly benefitted from his creative ideas and deep physics understanding, which is shown in this work. He has been always very patient and positive to help me step by step to complete my thesis successfully. Besides his knowledgeable help in the research, he is also a good friend to me. His enthusiasm breathes new life into our group and make us work as a family.

Secondly, I am grateful to all PHENIX collaboration colleagues, particularly the Muon Group for making this work possible. Dr. Tony Frawley had been closely working with us in my early stage of graduate studies and also gave useful suggestions on finalizing the results for my research work to be approved by the collaboration. Dr. Melynda Brooks and Dr. David Silvermy guided me in carrying out the data quality study and helped me understand the detector performance and simulations. Dr. Hugo Pereira has selflessly maintained the Muon Arm analysis software for a long time, making the data analysis possible. Dr. Mike Leitch, the MuTr expert, and Dr. Vince Cianciolo, the MuID expert,

helped me to understand the detectors and work out the analysis properly. Dr. Xiaorong Wang and Dr. Gobinda Mishra, who had been members in our working group earlier, had initiated this work and helped me get on track. Without all the efforts from these colleagues, this work would not be a success.

I would also like to acknowledge my committee members: Dr. Steven Manson, Dr. William Nelson, Dr. Brian Thoms and Dr. Douglas Gies (also Dr. Paul Wiita as my master's degree committee member) for their generous time to review and give suggestions on my work and thesis. Meanwhile, I appreciate the Physics and Astronomy department at the Georgia State University led by Dr. Richard Miller, together with the Physics Graduate Student Supervisor Dr. A. G. Perera, and staff members Mrs. Felicia Watts and Mrs. Yvette Hilaire who make great efforts to make a nice environment for the graduate students.

During my graduate studies at the Georgia State University, I have met and made friends with many people: Ms. Carola Butler, Christopher Cleven, Dr. Jun Ying, Dr. Hakmana Sanjeewa, Dr. Pushpa Wijesinghe, Dr. John Wilson, Dr. Murad Sarsour, Robert Zaballa, Christopher Oakley, Kanishka Dayananda, and Abhisek Sen. I am grateful for their friendship and help.

Finally, I am forever indebted to my parents Youdi Zhang and Yishen Qu, my sister Bo Qu and my wife Yiying Zhou for their understanding, endless patience, and encouragement when it was most required. Now it's your turn to be rewarded.

Thank you all.

# Table of Contents

# List of Tables

# List of Figures

# Chapter 1

# Introduction

The standard model states that the elementary particles of matter are comprised of quarks, leptons and their anti-particles. There are six flavors of quarks, namely *up*, *down*, *strange*, *charm*, *bottom*, and *top*. For example, the proton contains two up and one down quark, while the neutron contains one up and two down quarks. Not only does the quark carry electric charge, but also it carries color charge, which is a property of the strong interaction. [1]

The theory of the strong interaction is known as quantum chromodynamics (QCD). In this theory, the quarks interact with each other by exchanging gluons. The quarks are fermions of spin 1/2, and gluons are bosons of spin 1, in analogy to quantum electrodynamics (QED) where electrons are fermions (spin 1/2) and photons are bosons (spin 1).

Color charged particles (such as quarks) are always tightly bounded to each other, and therefore cannot be directly observed in experiment. This phenomena is called *confinement*. The interaction between bound quarks increases rapidly as the distance between

them increases, [2] which prevents them from being separated from each other. When two bound quarks are pulled far apart, new quarks will be created. A simple analogy would be of a spring: the stored energy increases as the the spring is stretched. The spring represents the gluon field while the two ends of the spring represent the quarks. If the spring is stretched so much that it breaks into fragments, two new ends will be created in each fragment but there are no free ends. On the other hand, the potential is found to decrease when quarks are very close to each other, which is called *asymptotic freedom*. This suggests that for short distance scales, or high momentum scales, the quarks and gluons are not confined.

One way to deconfine the quarks and gluons is to create a state of matter at extremely high energy density or temperature. This new state of matter is known as the *quark-gluon plasma* (QGP). [3] It is speculated in theory that the QGP may be formed in experiments by colliding heavy nuclei at relativistic energies. Such experiments are performed at the Relativistic Heavy Ion Collider (RHIC). Figure 1.1 shows the phases of a heavy ion collision. In the first image, two heavy ions approach one another at the speed of 99.95% the speed of light. The ions appear flat, instead of spherical, due to the Lorentz contraction. In the second image, the two ions collide, smashing into one another and then passing through each other. The hot, dense medium created by the collision "melts" the protons and neutrons and, for a brief instant (roughly $10^{-23}$ seconds after the collision), liberates the quarks and gluons, which is shown in the third image. Finally, thousands of particles form as the system cools, which can be used as probes of the QGP.

In 1986, Matsui and Satz predicted the suppression of heavy quarkonia (such as

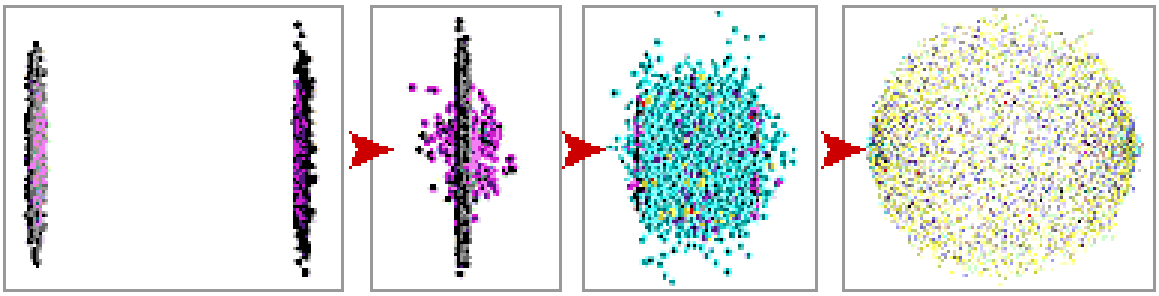

Figure 1.1: (color online) The phases of heavy ion collisions. [4]

$J/\psi$) production in heavy ion collisions as an unambiguous signature for the formation of the QGP. [5] $J/\psi$ suppression has been observed in the experiments at RHIC and the SPS. [6, 7] However, extensive measurements of $J/\psi$ production have shown pronounced suppression in proton-nucleus or deuteron-gold collisions where QGP formation is not expected. [8, 9, 10] In order to fully understand the $J/\psi$ production in the hot, dense nuclear medium, a careful study of its production in cold nuclei is very important.

The polarization of heavy quarkonia has long been recognized to provide crucial information on the quarkonium production mechanism. [11, 12] Measurements of $J/\psi$ polarization have been performed in several experiments. [13, 14, 15] In this dissertation, I describe $J/\psi$ polarization measurements conducted at the PHENIX experiment in proton+proton collisions at 200 GeV center of mass energy. In Chapter 2, the concept of a quarkonium is introduced, followed by the description of theoretical models of quarkonium production and polarization. In Chapter 3, the PHENIX experiment at RHIC is described. The data analysis is presented in Chapter 4. The results and discussion are given in Chapter 5, and the summary and conclusion in Chapter 6.

# Chapter 2

# Quarkonium Production

## 2.1 The Quarkonium

In analogy to the positronium (composed of an electron and a positron), a quarkonium is a hadronic bound state of a quark and antiquark. Usually quarkonium refers to charmonium (charm quark/anti-charm quark state) and bottomonium (bottom quark/anti-bottom quark state).

The first charmonium state that was discovered is $J/\psi$. [16, 17] It has the same quantum number as the photon ($J^P = 1^-$) and its mean lifetime is $7.2 \times 10^{-21}$ seconds. Its primary decay channel is to hadrons. It also has a lepton decay channel to $e^+e^-$ and $\mu^+\mu^-$, which can be measured from $e^+e^-$, $ep$ and $pp$ collision experiments. Another resonant S state, similar to $J/\psi$, but with a slightly higher mass is called $\psi^{'}(\psi(2S))$. The study of multiplicity in pion decays indicates that $J/\psi$ and $\psi(2S)$ decays are restricted by G-parity conservation, holding only for hadrons. Consequently, $J/\psi$ and $\psi(2S)$ are considered as hadrons of isospin 0 and G-parity -1. Particles with charge conjugation C = +1 in the the

P state were also found later and are called $\chi_c$. Table 2.1 and Fig. 2.1 show the properties and decays of the charmonia. The first bottomonium, called $\Upsilon$ was brought to light at Fermilab in 1977. [18] It is similar to the $J/\psi$ with mass 9.46 GeV. The excited states of $\Upsilon$ were also found later. The properties and decays of bottomonia are shown in Table 2.2 and Fig. 2.2.

Table 2.1: Properties of charmonia. [19]

| Meson | $n^{2S+1}L_J$ | $J_{PC}$ | Mass (GeV) |
|---|---|---|---|
| $\eta_c$ | $1^1S_0$ | $0^{-+}$ | 2.980 |
| $J/\psi$ | $1^3S_1$ | $1^{--}$ | 3.097 |
| $\chi_{c0}$, $\chi_{c1}$, $\chi_{c2}$ | $1^3P_{0,1,2}$ | $0^{++}, 1^{++}, 2^{++}$ | 3.415,3.511,3.556 |
| $h_c$ | $1^1P_0$ | $1^{+-}$ | 3.523 |
| $\eta_c(2S)$ | $2^1S_0$ | $0^{-+}$ | 3.594 |
| $\psi(2S)$ | $2^3S_1$ | $1^{--}$ | 3.686 |

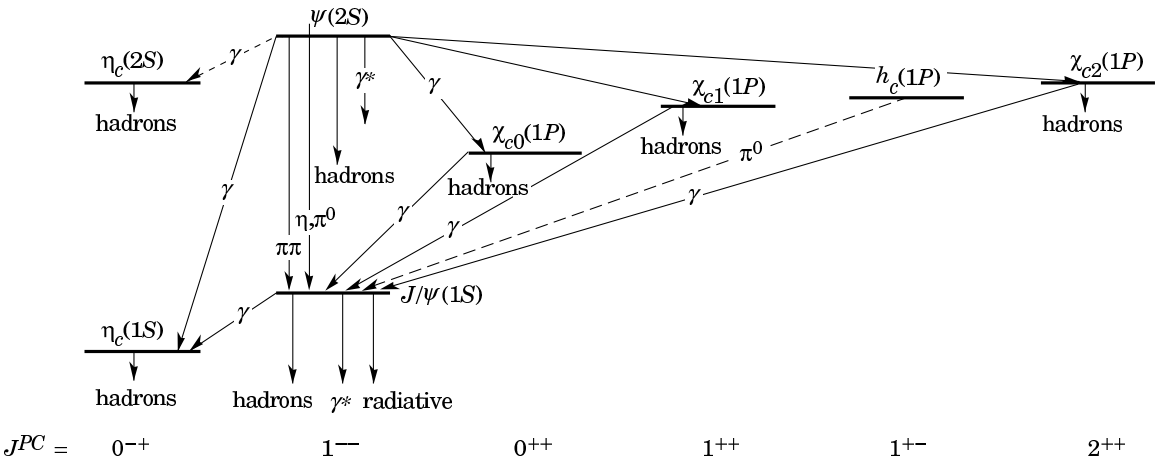


Figure 2.1: Spectrum and transitions of the charmonium family. [19]

The production and hadronization of quarkonium has been investigated for a long time but is still not clearly understood. It is complicated because it involves both pertur-

Table 2.2: Properties of bottomonia. [19]

| Meson | $n^{2S+1}L_J$ | $J_{PC}$ | Mass (GeV) |
|---|---|---|---|
| $\Upsilon(1S)$ | $1^3S_1$ | $1^{--}$ | 9.460 |
| $\chi_{b0}$, $\chi_{b1}$, $\chi_{b2}(1P)$ | $1^3P_{0,1,2}$ | $0^{++}$,$1^{++}$,$2^{++}$ | 9.860,9.893,9.913 |
| $\Upsilon(2S)$ | $2^3S_1$ | $1^{--}$ | 10.023 |
| $\chi_{b0}$, $\chi_{b1}$, $\chi_{b2}(2P)$ | $2^3P_{0,1,2}$ | $0^{++}$,$1^{++}$,$2^{++}$ | 10.232,10.255,10.269 |
| $\Upsilon(3S)$ | $3^3S_1$ | $1^{--}$ | 10.355 |

bative and nonperturbative aspects of QCD dynamics. Below is a brief description of the current models of quarkonium production, particularly for $J/\psi$ production.

## 2.2 Production Mechanisms

### 2.2.1 The Non-Relativistic QCD Factorization Method

The non-relativistic QCD (NRQCD) approach is the theory of QCD in the limit of $\Lambda_{QCD}/m \to 0$, where $\Lambda_{QCD}$ is the QCD coupling constant and m is the mass of the quarkonium. The much larger heavy-quark mass $m_Q$ than $\Lambda_{QCD}$ implies that the rates for heavy quarkonium decay and production can be calculated in perturbation theory. On the other hand, there are nonperturbative effects associated with the dynamics of the quarkonium bound state that invalidate the direct application of perturbation theory, for example, the hadronization of the $J/\psi$ from the charm quark and anti-quark pairs.

In order to make use of perturbative methods, the NRQCD factorization method has been developed to separate the short-distance/high-momentum, perturbative effects from the long-distance/low-momentum, nonperturbative effects through the use of effective field theory. [20, 21] The inclusive cross-section for the decay and direct production of a

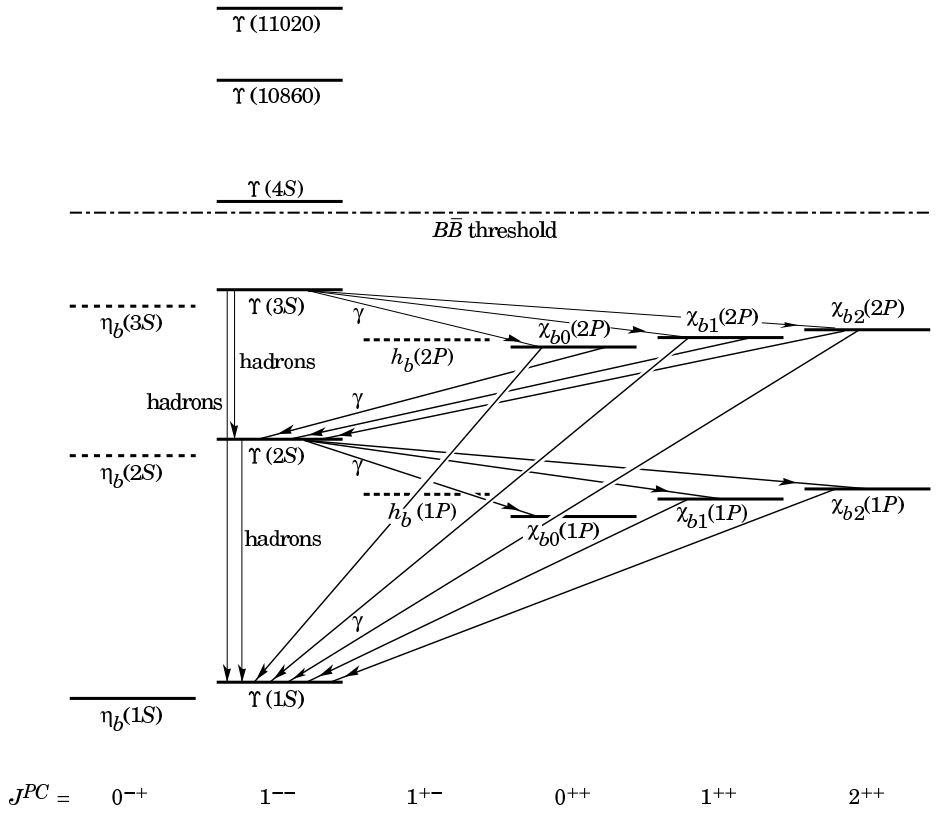


Figure 2.2: Spectrum and transitions of the bottomonium family. [19]

quarkonium H can be written as:

$$\sigma[H] = \sum_n \sigma_n(\Lambda) < \Theta_n^H(\Lambda) > \tag{2.1}$$

Here, $\Lambda$ is the ultraviolet cutoff of the effective theory, the $\sigma_n$ are short-distance coefficients, and the $< \Theta_n^H(\Lambda) >$ are vacuum-expectation values of four-fermion operators in NRQCD.

The short-distance coefficients $\sigma_n$ are the process-dependent partonic cross sections for producing of a $Q\overline{Q}$ pair. In hadron-hadron collision experiments, it is calculated from parton distributions of hadrons in the initial state. The $Q\overline{Q}$ pair can be produced in a color-singlet state or in a color-octet state. Its spin state can be singlet or triplet, and it

also can have orbital angular momentum. Because the scale of $Q\overline{Q}$ production is of the order $m_Q$ or greater, this matching can be carried out in perturbation theory.

The four-fermion operators in Eq. 2.1 create a $Q\overline{Q}$ pair in the NRQCD vacuum, projecting it onto a state that consists of a heavy quarkonium plus anything, and then annihilate the $Q\overline{Q}$ pair. The vacuum matrix element of such an operator is the probability for a $Q\overline{Q}$ pair to form a quarkonium plus anything. The matrix element contains all of the nonperturbative physics associated with evolution of the $Q\overline{Q}$ pair into a quarkonium state. In the hadron-hadron experiment at RHIC, the main processes of charmonium formation are:

- $g + g \rightarrow \psi + g$
- $q + g \rightarrow \psi + q$
- $q + \overline{q} \rightarrow \psi + g$

where q and g denote a quark and a gluon respectively and $\psi$ represents $J/\psi$ or $\psi(2S)$.

NRQCD power-counting rules allow one to organize the sum over operators in Eq. 2.1 as an expansion in powers of $v$, where $v$ is the typical heavy-quark velocity in the bound state in the quarkonium center of mass (CM) frame. [22] Through a given order in $v$, only a finite set of matrix elements contributes, and the number of independent matrix elements can be further reduced by making use of approximate relations, such as the heavy-quark spin symmetry and the vacuum-saturation approximation. [20].

A specific truncation corresponds to a particular model. In $J/\psi$ production at large transverse momentum ($p_T$) in hadron colliders, the color-octet terms of produced $c\overline{c}$ pairs are expected to dominate, so it is named as the "color-octet model" (COM).

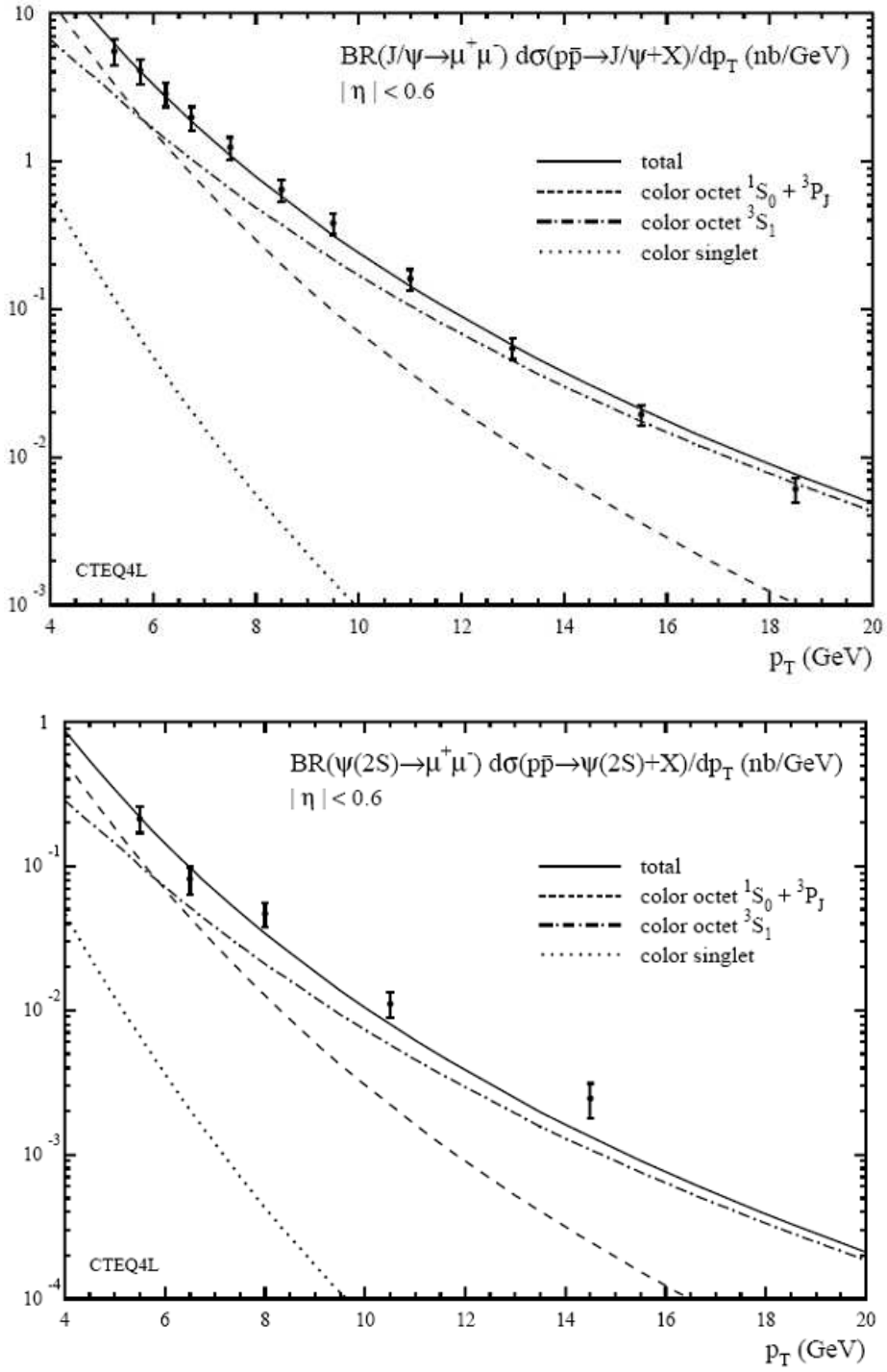


Figure 2.3: Fit of $J/\psi$ production data from Collider Detector at Fermi lab (CDF) ($\sqrt{s} = 1.8$ TeV, with pseudorapidity cut $|\eta| < 0.6$. [23]). Note the fit of color octet contributions to direct $J/\psi$ production data from CDF fits the data well. The color-singlet contributions are one order of magnitude less than the data.

The COM model allows the formation of $J/\psi$ from the dominant color-octet $c\bar{c}$ state by emitting soft gluons during the subsequent hadronization process to neutralize the color. As shown in Fig. 2.3, by including the leading color-octet contributions $c\bar{c}[8,{}^1S_0]$, $c\bar{c}[8,{}^3S_0]$ and $c\bar{c}[8,{}^3P_J]$, and adjusting corresponding non-perturbative parameters to fit the data, the COM model can reproduce the direct $\psi$ production data from CDF. [23]

The NRQCD factorization approach, with the color-octet model, implies transverse polarization of direct $J/\psi$ and $\psi$(2S) at large $p_T$. [24] But the polarization measurements from the CDF experiment contradict the COM predictions, which challenges the theory. This will be discussed in more detail in Section 2.3.

### 2.2.2 The Color-Singlet Model

The color-singlet model (CSM) has been proposed for a long time. [25] This model is the most natural application of QCD to heavy-quarkonium production in the high-energy regime. It can be obtained from the NRQCD factorization formula in Eq. 2.1 by only including color-singlet terms. The term that is retained is the one in which the quantum numbers of the $Q\overline{Q}$ pair are the same as those of the quarkonium. An assumption is that the color and the spin of the $Q\overline{Q}$ pair does not change during the binding and hadronization processes. Since the final physical states are colorless, it is required that the pair must be produced in a color-singlet state.

The CSM model was applied to the production of $J/\psi$ and $\eta_c$ in B-meson (containing bottom quarks) decays [26, 27, 28] and to the production of $J/\psi$ plus a gluon [29, 30, 31] through two-gluon fusion and photon-gluon fusion. This model was taken seriously until around 1995, when experiments at the Tevatron showed that it under-predicts the cross-

section for prompt charmonium production in $p\bar{p}$ collisions by more than an order of magnitude, even including the CSM fragmentation contribution. [32, 33]

In a recent development of the theory, H. Haberzettl and J.P. Lansberg argue that the S-channel cut contribution to $J/\psi$ hadroproduction can be significantly larger than the usual cut contribution of the CSM when one includes interactions of the $c\bar{c}$ pair which binds the quarkonium and emits the final-state gluon. [34]

### 2.2.3 The Color-Evaporation Model

The color evaporation model (CEM) was first proposed in 1977 [35, 36] and has had considerable phenomenological success. In the CEM, the cross-section for a quarkonium state H is considered to be a fraction ($F_H$) of the cross-section for producing $Q\overline{Q}$ pairs with invariant mass below the $M\overline{M}$ threshold, where M is the lowest mass meson containing the heavy quark Q. The $Q\overline{Q}$ pair is assumed to neutralize its color by interaction with the collision-induced color field, referred to as "color evaporation". The fractions $F_H$ are assumed to be universal. Once they are determined empirically, they can be used to predict the cross-sections in other processes and in other kinematic regions. There is a correspondence between the CEM and the NRQCD factorization approaches phenomenologically. In NRQCD, the production matrix element $< \Theta_n^H(\Lambda) >$ is proportional to the expectation value of the operator to project on hadronic state H; while in CEM, the fraction $F_H$ is proportional to the expectation value of the formation of $Q\overline{Q}$ states with invariant mass less than $2m_M$. [37]

The CEM model can describe reasonably well the normalization and the shape of the prompt charmonium cross-section at the Tevatron. [38, 39] But it also has drawbacks.

The most basic prediction of the CEM model is that the ratio of the cross-sections for any two quarkonium states should be constant, independent of the process and the kinematic region. But the ratio of the cross sections for $\chi_c$ and $J/\psi$ differs significantly in photoproduction and hadroproduction, which challenges its prediction. Meanwhile, the assumption of the randomization of the $Q\overline{Q}$ spin also implies simple spin-counting ratios for the cross sections of the direct production of quarkonium states in the same orbital angular momentum multiplet. For example, the CEM with spin randomization predicts that the direct-production cross-sections for charmonium satisfy $\sigma_{dir}[\eta_c] : \sigma_{dir}[J/\psi] = 1 : 3$ and $\sigma_{dir}[\eta_{c0}] : \sigma_{dir}[\eta_{c1}] : \sigma_{dir}[\eta_{c2}] = 1 : 3 : 5$. However, deviations of these ratios have been observed in hadron collision experiments. Furthermore, this model is unable to give quantitative information about the polarization of the quarkonium, which is a key test for any model.

### 2.2.4 The Uncertainties and Tests of the Models

In practical calculations of the rates of quarkonium decay and production, a number of significant uncertainties arise. In many instances, the series in the coupling constant $\alpha_s$ and the velocity $v$ in the factorization formula in Eq. 2.1 converge slowly, and the uncertainties from their truncation are large, sometimes 100% or more. In addition, the matrix elements are often poorly determined, either from phenomenological or lattice calculations, and the important linear combinations of matrix elements vary from process to process, making tests of universality difficult. There are also large uncertainties in the heavy-quark masses (approximately 8% for $m_c$ and approximately 2.4% for $m_b$) that can be very significant for quarkonium production rates that are proportional to a large power of the mass.

Meanwhile, the next to leading order (NLO) QCD and relativistic corrections can be important for the production mechanism. The development of the models is discussed by several authors. [40, 41]

One way to test the validity of these models is to measure the ratio of the cross section from different states. Large uncertainties from the theoretical predictions and the experimental measurements can be canceled out in the ratios of cross-sections. Examples in charmonium production are the ratio of the inclusive cross-sections for $\psi(2S)$ and $J/\psi$ production and the ratio $R_{\chi_c}$ of the inclusive cross-sections for $\chi_{c1}$ and $\chi_{c2}$ production. Another way is to measure the quarkonium polarization, which will be discussed next.

## 2.3 The Measurement of Polarization

### 2.3.1 Angular Distribution

The quarkonium polarization has been for a long time recognized as the crucial test for its production mechanism. [11] In particular, predictions for the polarization are largely independent of the detailed parton distribution, and also insensitive to normalization. Meanwhile, the large systematic uncertainties in experimental measurements can be canceled out when measuring the ratios of cross-sections for the production of different spin states of the same quarkonium.

Polarization measurements are typically done through a parametrization of the polar angular distribution of the quarkonium's decay leptons in its rest frame. [42] The angular distribution is given by,

$$\frac{d\sigma(\psi \to l^+l^-)}{d\cos\theta} \propto 1 + \lambda\cos^2\theta \tag{2.2}$$

Where $\theta$ is the angle between the positive decay lepton ($l^+$) momentum and the chosen polarization axis in the quarkonium rest frame. The selection of the polarization axis depends on the process. [43] In this analysis, I choose the helicity frame. In this frame, the polarization axis is chosen as the momentum direction of the quarkonium in the center of mass frame of the colliding system as shown in Fig 2.4. The detailed Lorenz transformation

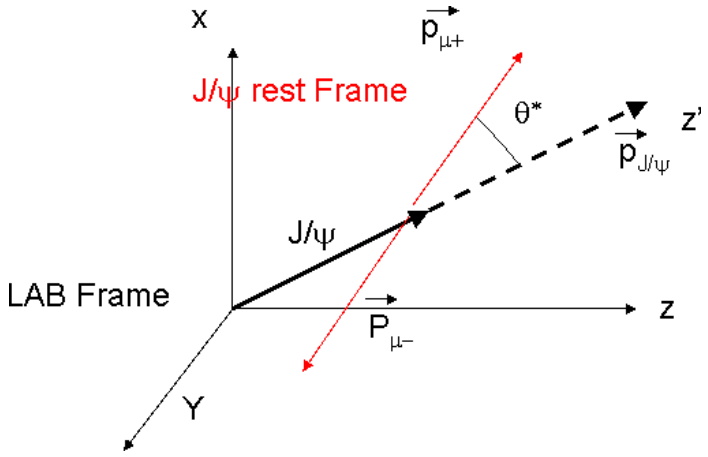


Figure 2.4: The $J/\psi$ helicity frame. The polarization angle $\theta$ is defined between the positive decay lepton momentum direction in the $J/\psi$ rest frame and the momentum direction of $J/\psi$ in the lab frame.

of the quarkonium (e.g. $J/\psi$) momentum between the rest frame and the center of mass frame is given in Appendix B. The $\lambda$ is the polarization parameter, where $\lambda = 0$ indicates non-polarization, $\lambda = 1$ corresponds to complete transverse polarization, and $\lambda = -1$ to complete longitudinal polarization as shown in Fig. 2.5.

### 2.3.2 Model Predictions of Quarkonium Polarization

The analysis of $J/\psi$ and $\psi(2S)$ polarization at large transverse momentum is one of the most decisive tests of the NRQCD factorization approach. [23, 24, 44, 45, 46, 47, 48]

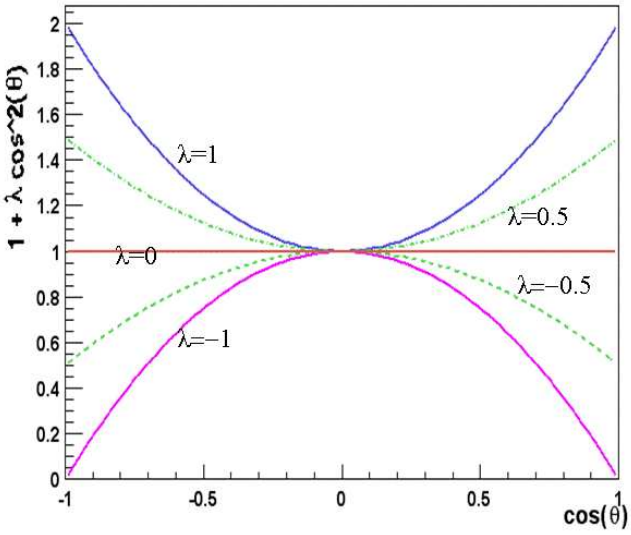


Figure 2.5: Angular distributions for different $\lambda$ values. $\lambda = 0$: non-polarization, $\lambda = 1$: complete transverse polarization, $\lambda = -1$: complete longitudinal polarization.

At large $p_T$, the direct $J/\psi$ and $\psi(2S)$ cross sections should be dominated by gluon fragmentation, a process in which the quarkonium is formed in the hadronization of a gluon that is created with large transverse momentum. When $p_T \gg 2m_c$ the fragmenting gluons are effectively on-shell and the intermediate heavy quark pairs are transversely polarized. According to the standard NRQCD power counting rules, $c\bar{c}$ evolves into $J/\psi$ or $\psi(2S)$ predominantly through a double chromoelectric transition which preserves the heavy quark spin. The dominance of gluon fragmentation into color-octet charm quark pairs at large $p_T$, along with NRQCD spin-symmetry, thus imply transversely polarized $J/\psi$ and $\psi(2S)$ at large transverse momentum. In the low and medium $p_T$ regions, the color-octet $^1S_0$ and $^3P_J$ fusion processes are dominant, which predict nonpolarization of $J/\psi$ and $\psi(2S)$. [23]

In the CSM model, the heavy quark spin symmetry relates the CSM matrix elements with the angular momentum, thus it gives nontrivial predictions for polarization.

In general, the predictions do not show dramatic polarization. [45] Recently, by taking into account the next to leading order QCD corrections via the CSM mechanism, it is possible that the $J/\psi$ produced at large $p_T$ is longitudinal polarized. [40, 41]

The color-evaporation model assumes that there are unsuppressed gluon emissions from the $c\bar{c}$ pair during hadronization that randomize spin and color, and consequently the CEM model predicts unpolarized quarkonium. [39]

As mentioned in Section 2.2.4, calculations of the production and polarization of quarkonium can involve large uncertainties. Further discussions can be found in Kramer's paper. [49]

### 2.3.3 Quarkonium Polarization Measurements from Experiments

Quarkonium polarization has been measured in hadron-hadron collision experiments. The CDF experiment of $p\bar{p}$ collisions at the Tevatron measured $J/\psi$ and $\psi(2S)$ polarization as a function of $p_T$, as shown in Fig. 2.6. The measurements were done in the region of $p_T$ >5 GeV and $|y| < 0.6$. The $J/\psi$ polarization parameter value is negative over the entire measured $p_T$ range, and becomes increasingly negative (favoring longitudinal polarization) as $p_T$ increases. For $\psi(2S)$, the central value of the polarization parameter is positive at small $p_T$. When $p_T$ increases, it becomes negative. It is noted that the uncertainties are large for $\psi(2S)$ polarization measurements, but the trend is consistent with the result from the measurement of $J/\psi$ polarization. The band in the figure shows the NRQCD factorization prediction. The measured $J/\psi$ and $\psi(2S)$ polarizations are in strong disagreement with the NRQCD predictions.

Quarkonium polarization has also been measured in fixed target experiments. The

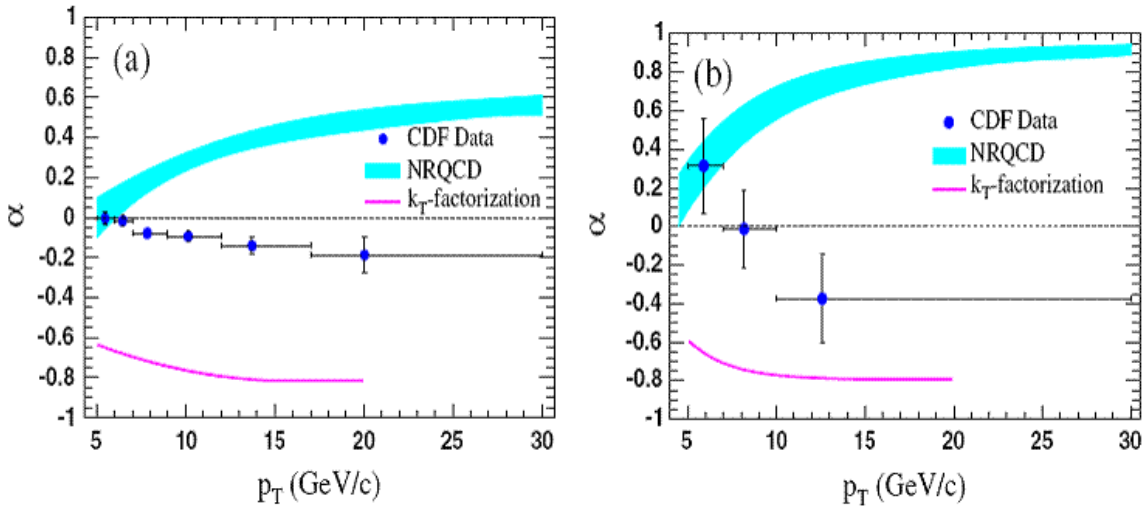


Figure 2.6: (a) $J/\psi$ and (b) $\psi(2S)$ polarization measurements from CDF at Fermi lab. [14]

experimental results for the $J/\psi$ polarization are summarized in Table 2.3. In these experiments, the $J/\psi$ transverse momentum is smaller than 5 GeV. In general, the results are consistent with $\lambda = 0$.

Table 2.3: Results of the $J/\psi$ polarization measurement in fixed target experiments.

| Experiment | Beam/Target | Beam Energy/GeV | $\lambda$ |
|---|---|---|---|
| E537 [50] | ($\pi$, p)+(Be, Cu, W) | 125 | 0.024 – 0.032 |
| E672/706 [51] | p+Be | 530 | 0.01 $\pm$ 0.15 |
| E672/706 [51] | p+Be | 800 | -0.11 $\pm$ 0.15 |
| E771 [51] | p+Si | 800 | -0.09 $\pm$ 0.1 |
| E866 [13] | p+Cu | 800 | 0.069 $\pm$ 0.08 |

The NA60 experiment has carried out a measurement of $J/\psi$ polarization in In-In collisions at the CERN Super Proton Synchrotron accelerator (SPS). [15] The preliminary results indicate that no significant $J/\psi$ polarization has been observed as a function of

centrality, $p_T$ or the rapidity.

# Chapter 3

# The Experiment

In this chapter, I give a general description of the experimental apparatus setup used for $J/\psi$ polarization measurement. I start by introducing the Relativistic Heavy Ion Collider (RHIC), followed with a description of the PHENIX detector subsystems, the trigger setup and the data acquisition system. The offline data reconstruction procedure and muon particle reconstruction algorithm are given at the end of the chapter.

## 3.1 The RHIC Complex

The RHIC, located at Brookhaven National Laboratory, is the first relativistic heavy ion collider in the world. It is capable of accelerating various nuclei from protons to gold nuclei, with a maximum energy of 100 GeV per nucleon for heavy ions and 250 GeV for protons. Figure 3.1 shows the layout of the RHIC facility. The accelerators for heavy ion collisions consist of Tandem, Booster and Alternating Gradient Synchrotron (AGS). The AGS was operated in 1980's for the fixed target experiments and now serves as the injector

to the RHIC rings. For proton+proton collision, the accelerators consist of LINAC, Booster and AGS.

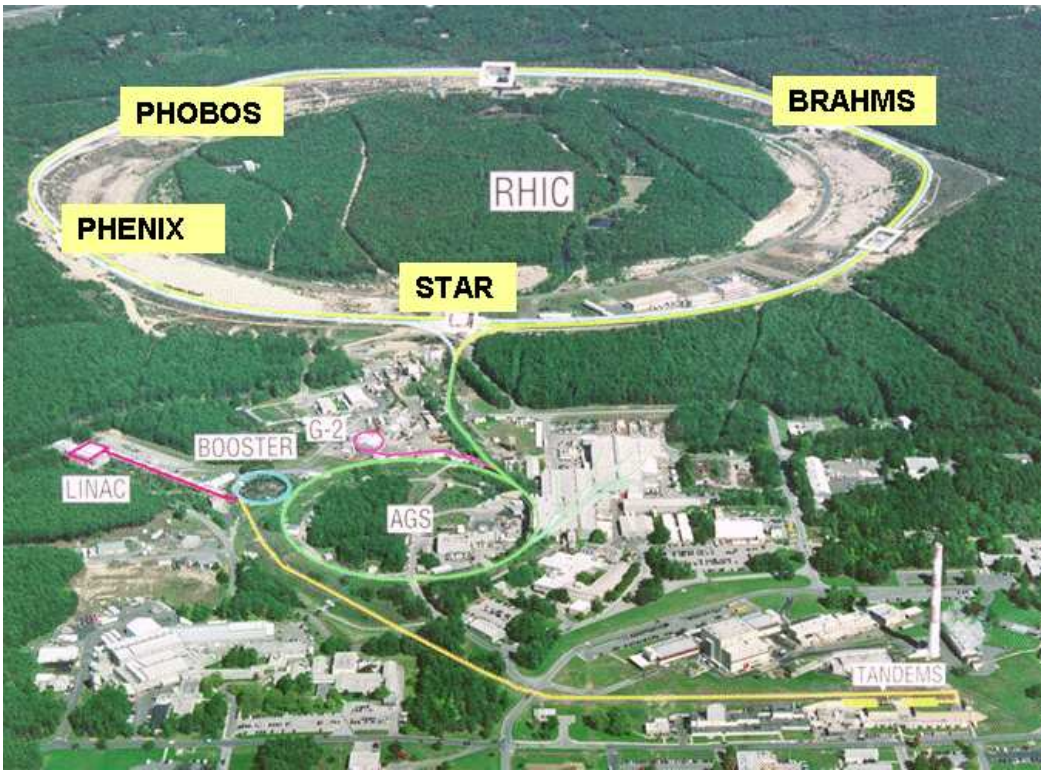


Figure 3.1: The Relativistic Heavy Ion Collider Facility.

RHIC has two independent rings. They are 3.83 km long and have about 1000 super-conducting magnets. [52] The beam particles are accelerated to 99.95% of the speed of light in the two rings and collide at six interaction regions (IR). There were four experiments operated at RHIC: BRAHMS, PHENIX, PHOBOS, and STAR. BRAHMS (Broad RAnge Hadron Magnetic Spectrometers Experiment) is designed to measure inclusive momentum spectra of identified charged hadrons over a wide range in rapidity and transverse momentum. [53] PHENIX (Pioneering High Energy Nuclear Interaction eXperiment) is de-

signed specifically to measure electrons, muons, and photons from rare processes at a high event rate. [54] PHOBOS, named after a moon of Mars, is designed to measure low $p_T$ charged particle multiplicity. [55] STAR (Solenoidal Tracker At RHIC) is designed to use large time projection chamber to track charged particles over a large geometric acceptance at a relatively low rate. [56] The four experiments started to take data in 2000. By 2006, the BRAHMS and PHOBOS had achieved their physics goals and have been decommisioned.

## 3.2 The PHENIX Experiment

PHENIX is one of the largest experiments at RHIC. It is designed to study the properties of extremely hot and dense matter created by heavy ion collisions at RHIC. [57] It can also be used to study the spin structure of proton. It has the ability to measure leptons, photons and hadrons with good mass resolution and particle identification capabilities. [57] The PHENIX schematic layout is shown in Fig. 3.2

PHENIX utilizes a variety of detector technologies. A set of global detectors is constructed to characterize the basic nature of collisions, like vertex position and collision centrality. A pair of central spectrometers (Central Arms) is built to detect electrons, hadrons, and photons. The Central Arms stand in layers and surround the beam pipe in the East and West directions. They cover the middle rapidity acceptance. A pair of forward spectrometers (Muon Arms) is built to measure muons. The Muon Arms intersect with the beam pipe in the North and South directions. They cover the forward and backward rapidities with full azimuth. In this thesis, the data from muon arm detectors have been analyzed. In the followed sections, the descriptions of the detectors are given.

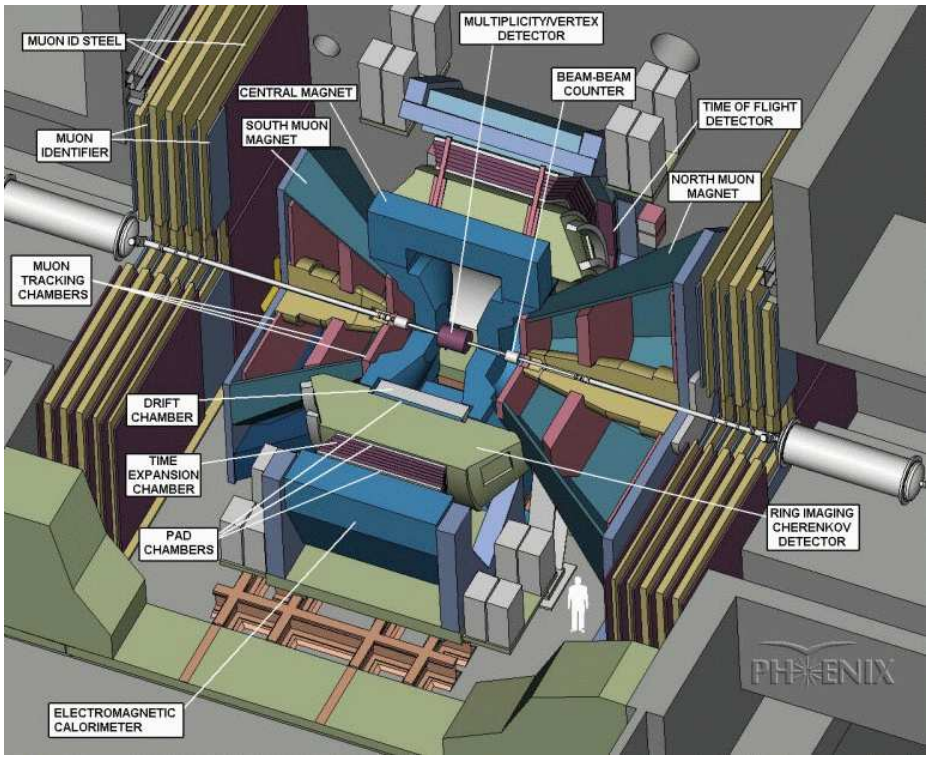


Figure 3.2: The PHENIX schematic layout. A wedge of the detector has been cut away to show the internal structure. Note the detector size compares to the size of an adult in right hand corner.

## 3.3 The Global Detectors

The global detectors consist of Beam-Beam Counters (BBC) and Zero-Degree Calorimeters (ZDC) [58] as shown in Fig. 3.3. The two BBC detectors are located at $\pm 1.44$ m from the beam collision point. They cover a $2\pi$ azimuthal and $3.0 < |\eta| < 3.9$ rapidity range. The BBC provides a measurement of the flight time of forward charged particles to determine the time of a collision event. It also provides the information to determine the collision vertex position and collision centrality. The trigger efficiency of the BBC is close to 75% with an event vertex between $\pm 30$ cm. The ZDC is used to detect neutral

particles from the most peripheral collisions. It is also used for triggering and centrality determination.

## 3.4 The Central Arms

The Central Arms are designed to detect electrons, hadrons, and photons. They are comprised of tracking systems for charged particles and an electromagnetic calorimeter [57] as shown in Fig. 3.3. The calorimeter is the outermost subsystem of the Central Arms. It provides measurements of the energies and spatial positions of photons and electrons. The tracking system uses three sets of Pad Chambers (PC1/2/3) to provide three-dimensional space points needed for pattern recognition. The Drift Chambers (DC) provide good momentum resolution with tracking ability. The Time Expansion Chamber (TEC) in the East arm provides additional tracking and particle identification. The Time-of-Flight (ToF) and Ring-Imaging Cherenkov (RICH) detectors also provide particle identification.

## 3.5 The Muon Arms

The Muon Arms are designed to measure muons which come from vector meson and open heavy quark decays. [57] The current upgrade will play an important role in the RHIC spin program through the detection of single high $p_T$ muons resulting from W decays. [59]

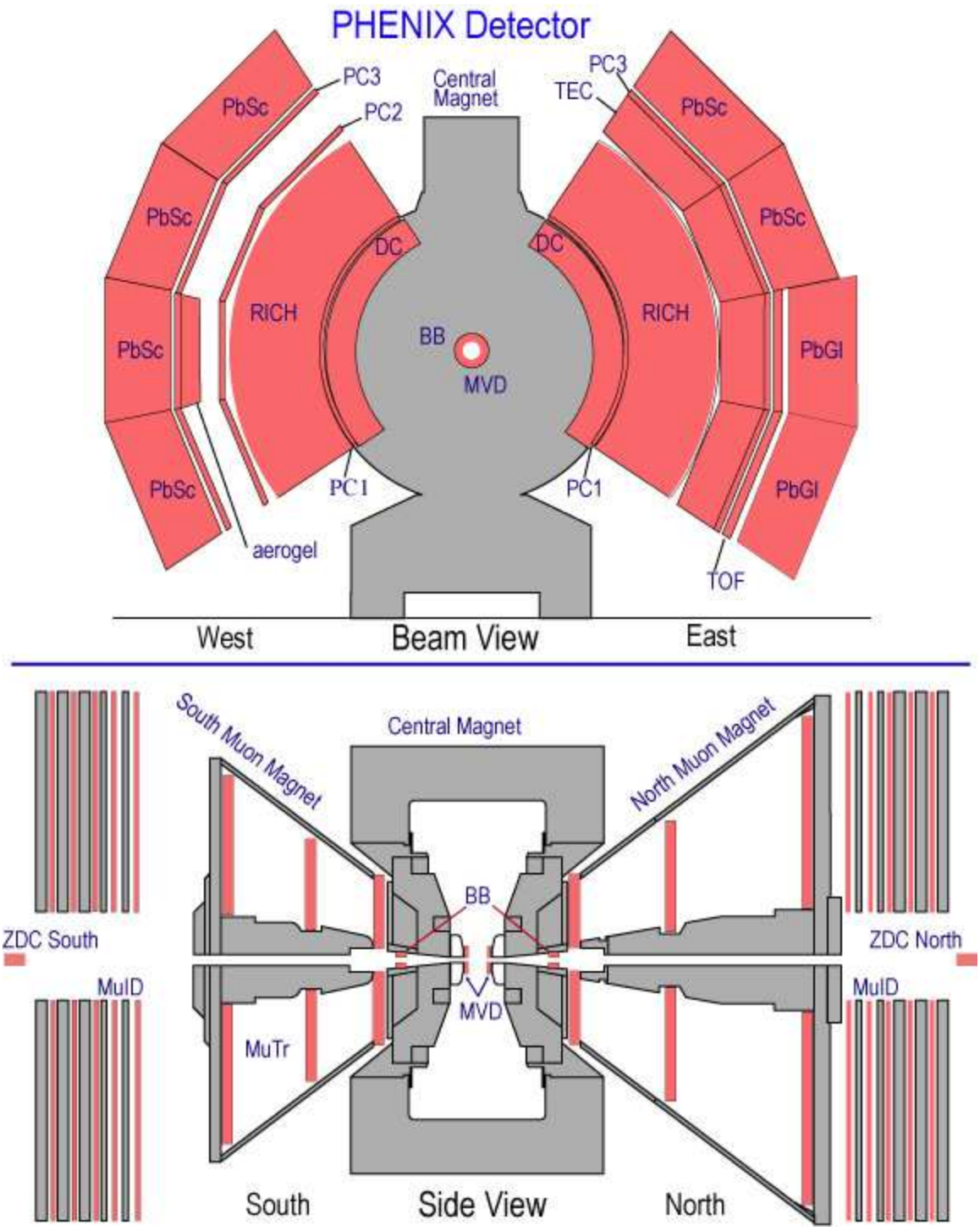


Figure 3.3: PHENIX detector configuration for Run 2005. The Central Arms are shown in the upper panel and the Muon Arms are shown in the lower panel.

The Muon Arms, as shown in Fig. 3.3, consist of two independent spectrometers on either side of the beam interaction region along the direction of the collision axis. Each arm is composed of a muon magnet and two subsystem detectors: the muon tracker (MuTr) and the muon identifier (MuID). The forward (North) and the backward (South) arms are mostly identical in construction except for the length in the z-direction. The South MuTr is 1.5 m shorter in z and has a slightly smaller angular acceptance than the North MuTr in order to facilitate removal from the experiment hall. The acceptance coverage for North arm is $1.1 \leq \mathrm{y} \leq 2.4$ and for South arm is $-2.2 \leq \mathrm{y} \leq -1.2$.

In order to track and identify muons, the detector must provide a good rejection of hadronic background, for example pions and kaons, with a rejection factor of $10^4$. Several hadron absorbers have been installed. The first absorber is of 60 cm thick low-carbon steel and 20 cm thick brass, located between the collision point and active detectors along the beam axis. The first active detector, MuTr is comprised of three momentum tracking stations in a radial magnetic field. The MuTr is followed by the Muon Identifer (MuID). It consists of 5-layers of gas gaps interleaved with 4 steel absorbers, which aids in identifying and differentiating muons. There is also a thick steel plate (muon magnet backplate) between the MuID and the MuTr to further reduce the background. Figure. 3.4 shows the integrated nuclear interaction length as a function of the distance from the collision vertex. The minimum longitudinal momentum for a muon to reach the last MuID gap (gap 5) is about 2.5 GeV.

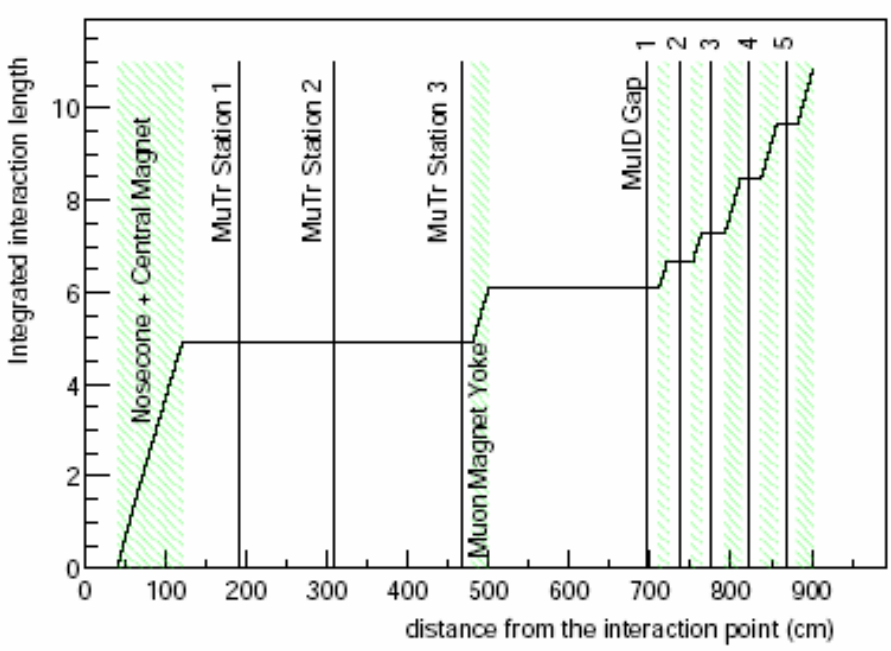


Figure 3.4: Muon integrated interaction length versus the absorbers. The plots is for the South muon arm. The North muon arm is the same except for the interaction length added by the magnet yoke.

### 3.5.1 The Muon Tracker

The MuTr detectors are enclosed in the muon magnet frame as shown in Fig. 3.5 The muon magnet provides a magnetic field in the radial direction so that the charged particles from the vertex bend in the azimuthal direction. The MuTr can provide precise momentum information for muon particles.

Each MuTr contains three cathode strip chamber (CSC) tracking stations as shown in Fig. 3.6. The stations are built in the shape of octants and divided into eight sections equally, while station 1 is divided into four sections.

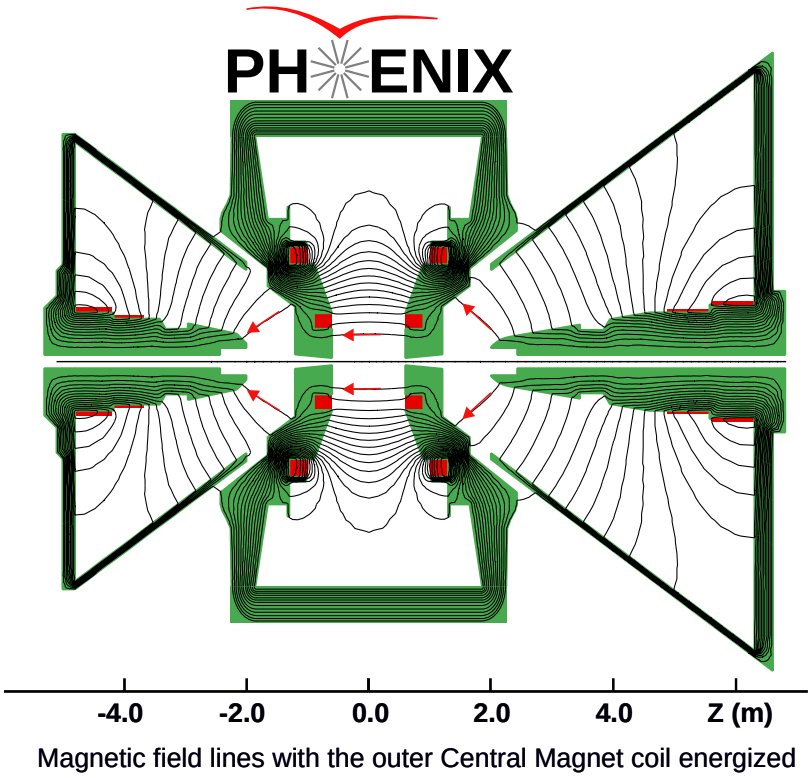


Figure 3.5: Magnetic field of the muon and central magnets. Note that the muon magnetic field is in the radial direction which bends the charge particles in the azimuthal direction.

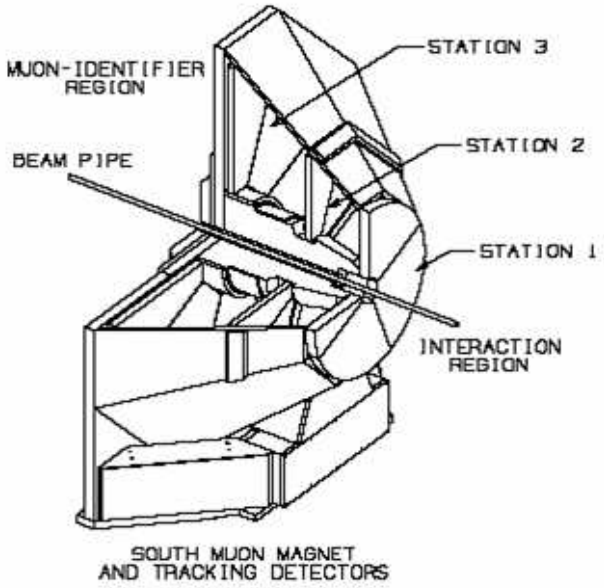


Figure 3.6: Sketch of south arm MuTr. It contains three cathode strip chamber (CSC) tracking stations. A wedge of the detector has been cut away to show internal structure. The beam pipe is also shown in the figure.

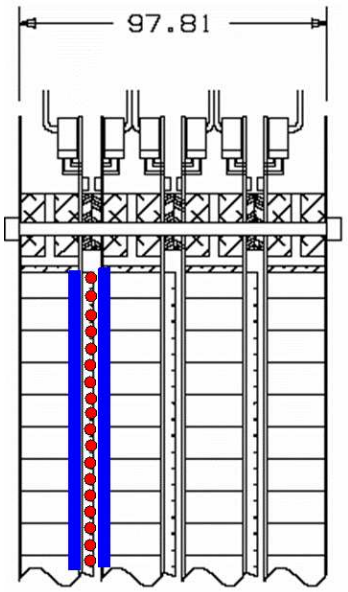


Figure 3.7: (color online) Cross section of MuTr station 1. There are three gaps, each consisting of two cathode-strip plane (blue) and one anode-wire plane (red).

Each station is made of multiple gaps, stations 1 and 2 consisting of three gaps and station 3 consisting of two gaps. Each gap is composed of two cathode-strip planes and one anode-wire plane as shown in Fig. 3.7. The cathode strips are aligned in the radial direction while the anode wires run in the azimuthal direction. Only the cathode strips are read out. In order to determine the three dimensional muon track position and to reject ghost tracks, the radial directions of cathode strips in the same gap run differently. One plane of strips (called the straight plane) runs perpendicularly to the anode-wire plane. The others (called the stereo plane) are rotated by a small angle ($< 12^o$) with respect to the straight plane. The resolution of the straight plane is about 100 $\mu m$ which fulfills the requirement for the muon momentum resolution measurement, while the resolution of the stereo planes is about 300 $\mu m$. Table 3.1 lists the rotated angle values for each plane. An example of the structure of the three gaps in station 1 is shown in Fig. 3.8.

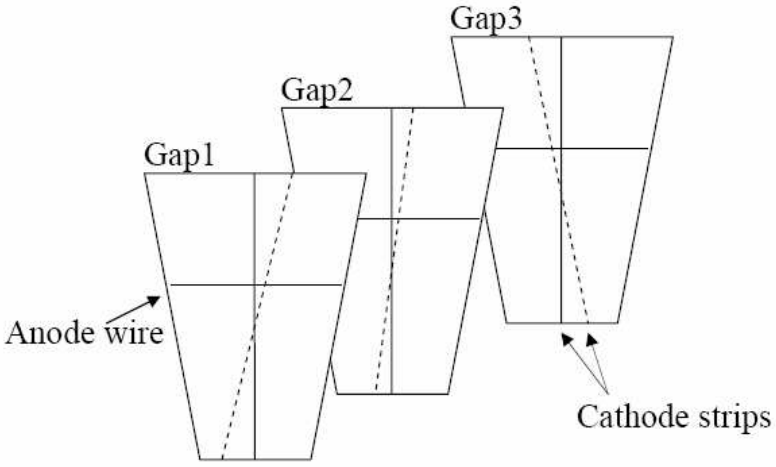


Figure 3.8: Illustration of the structure of a Muon tracker station 1 octant. The anode wire plane is between two cathode planes in each gap. Strips in stereo cathode planes are shown as dashed lines.

Table 3.1: The rotation angles of the stereo plane relative to the straight plane in MuTr stations. Positive signs represent the positive $\phi$ angle (counter-clockwise)

| Station | Gap | Angle (degree) |
|---|---|---|
| 1 | 1 | -11.25 |
| | 2 | +6 |
| | 3 | +11.25 |
| 2 | 1 | +7.5 |
| | 2 | +3.75 |
| | 3 | + 11.25 |
| 3 | 1 | -11.25 |
| | 2 | -11.25 |

To maintain the momentum resolution, an optical alignment system was installed to calibrate initial placement of the chambers, and to monitor displacements of the chambers to $\pm 25\ \mu m$. For each octant chamber, there are seven sets of optical alignment devices, each consisting of an optical fiber light source at station 1, a convex lens at station 2, and a CCD camera at station 3. The alignment of the MuTr is done octant to octant in the different stations relative one another.

The MuTr chambers are operated with a 0.5:0.3:0.2 mixture of Ar:CO2:CF4 non-flammable gas at 1.85 kV high voltage. This mode of operation provides a gain of $2 \times 10^4$. The typical charge deposited by a minimum ionizing particle in the CSC is about 100 electrons. [60] This results in a total cathode charge of 80 fC. Four ADC samples are read out from each cathode strip. The charge distribution is used to determine the muon track position. [61] A calibration system has been implemented to inject pulses to the chambers for measuring the gain and pedestal of every strip.

The MuTr Front End Electronics (FEE) [57] is the electronic readout interface between the MuTr chambers and the PHENIX Data Acquisition (DAQ) system which

is presented in Section 3.7. The electronics continuously amplify and store analog hit information from the chamber cathodes. Upon receipt of a Level-1 trigger from the PHENIX granule timing module (GTM), stored samples from all channels are digitized and the results are sent to the PHENIX data collection module (DCM) to be integrated for offline analysis.

### 3.5.2 The Muon Identifier

In principle, physical measurements (like the invariant mass and $p_T$ of vector mesons) in proton+proton collisions can be achieved by only using the MuTr detector. However, for heavy ion collisions (Au+Au), the background is so high that the measurement is impossible. As described previously, approximately two orders of magnitude (100) of background suppression can be achieved when particles from the vertex pass through absorbers in front of the Muon Arms (the Central Magnet pole pieces) and the return yoke of the Muon Magnets. But this still requires further reduction of the punch-through hadron background by a fact of about 30. Also, it is not feasible to implement the muon Level-1 trigger in the MuTr detector to measure the rare process. So a detector called MuID is designed to meet those requirements.

The MuID detector consists of 4 layers of large steel absorber plates as shown in Fig. 3.3. The first two layers are 10 cm thick and the other two are 20 cm thick. Together with the muon magnet backplate, they totally provide 90 cm (5.4 hadronic interaction lengths) of steel to make the punch-through probability for pions of up to 4 GeV 3% or less, which meets the requirement of suppression for the pair background. The 5 gaps created by the absorbers are instrumented with the MuID active detector planes (called MuID gaps). Segmentation of the gaps into multiple layers improves the detection of low momentum

muons, which increases the acceptance for the $\phi$ meson.

Each MuID gap consists of six panels as shown in Fig. 3.9. They are labeled from 0 to 5 arranged around the square hole where the beam pipe passes through. Panels 0, 2, and 4 lie on the same surface which is 10 cm closer to the vertex than the other panels. The acceptance reaches down to $10^o$ except at the four corners of the square beam hole. The overlap of each panel on the edge minimizes the dead area due to the panel frames.

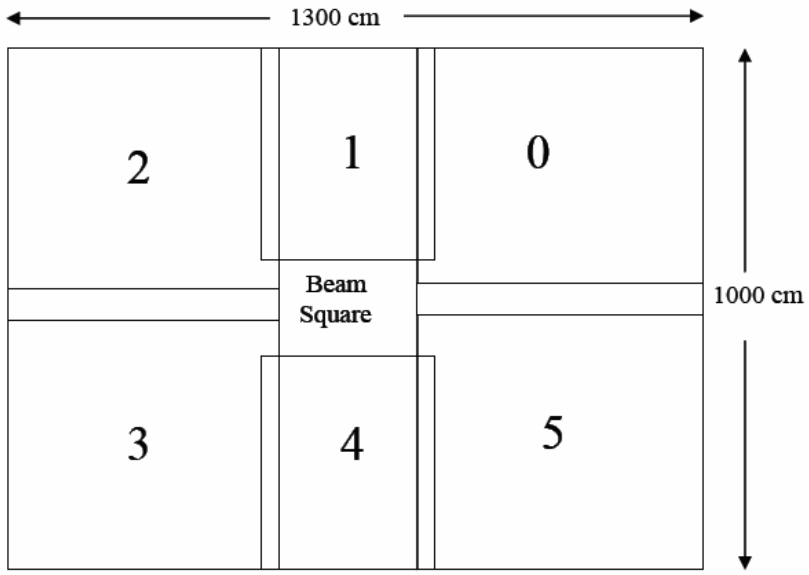


Figure 3.9: MuID layout

The panels consist of Iarocci type streamer tubes [62] inside aluminum boxes. The tubes are installed in horizontal and vertical orientations as shown in Fig. 3.10. For each orientation there are two layers of tubes which are staggered by one half-cell (5 mm). The two layer tubes are read out as a single-channel and called a two-pack. Compared to a single tube, this two-pack configuration allows a significant increase in efficiency due to the

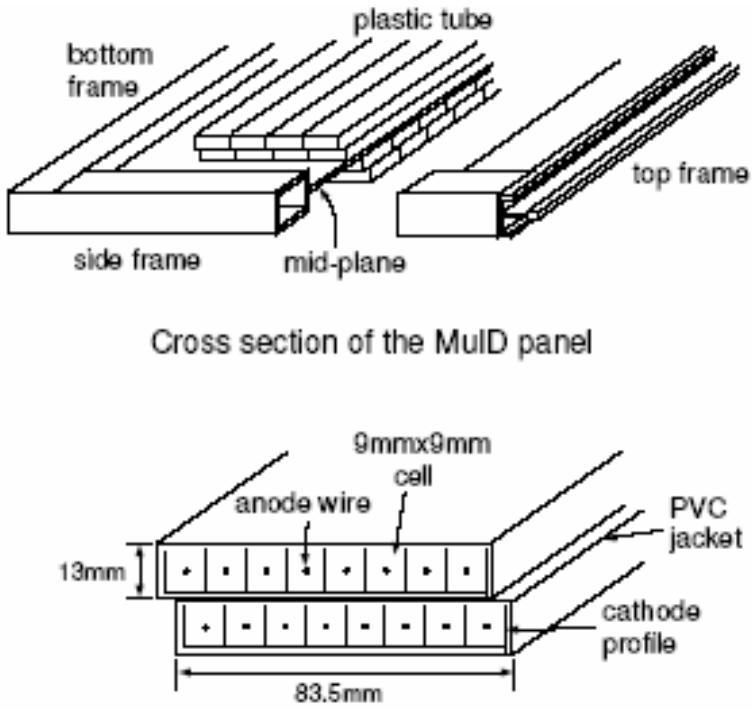


Figure 3.10: MuID tube configuration. The tubes are installed in horizontal and vertical orientations inside an aluminum frame as shown in the upper panel. Tubes with different orientations are mounted on opposite sides of a 1/8" aluminum mid-plane. The two-pack MuID tube is shown in the lower panel.

large overlap of active area and the minimal overlap of inactive area.

A gas mixture of $CO_2$ and up to 8% isobutane is fed into the tube for primary detector operation. $N_2$ is fed into the aluminum enclosure of each panel in order to keep the chamber electronics dry and clean, and to dilute the flammable gas component in case of a tube leak. The gas system runs in a recirculation mode.

Signals from the two-pack tubes are first amplified to reduce noise. After digitization and synchronization, they are sent to 9U electronic crates which have readout cards (ROC) and to the interface of the MuID and the PHENIX data acquisition system. [57] Upon receipt of a Level-1 acceptance signal the data collection module DCM interface assembles

and ships out the data.

## 3.6 The Triggers

The minimum bias trigger provided by BBC together with the MuID Local Level-1 trigger are used in the data taking for the Muon Arms. The BBC trigger requires that two photomultiplier tubes in each BBC fire, and the event z-vertex is between ±30 cm. [6] The MuID Local Level-1 trigger for muon pair selection requires that at least two muons penetrate the MuID. One muon must penetrate the entire MuID, while the second has a minimum penetration depth of 3 out of the 5 MuID absorber planes. [63] This trigger efficiently selects the rare $J/\psi$ events.

## 3.7 Data Acquisition System

PHENIX is designed to measure collisions at a high event rate. This brings a big challenge to the data acquisition system (DAQ) [64]. A sketch of the DAQ, as briefly described below, is shown in Fig. 3.11.

Each detector subsystem is equipped with a Front End electronics Module (FEM) which converts detector signals into digital event fragments with standard format. This involves analog signal processing with amplification and shaping to extract the optimum time and/or amplitude information. It also provides waiting time for trigger input by storing data in the buffer. When FEM is in the synchronizing status, a data sample from a few fast detectors is sent out to subsystem specific Local Level-1 (LLVL1) trigger hardware, which again sends a small number of bits which characterize the data to the Global Level-1 (GL1)

trigger boards to make a trigger decision. Within every 106 ns beam crossing time, the Granual Timing Modules (GTMs) send the request to FEM for the events.

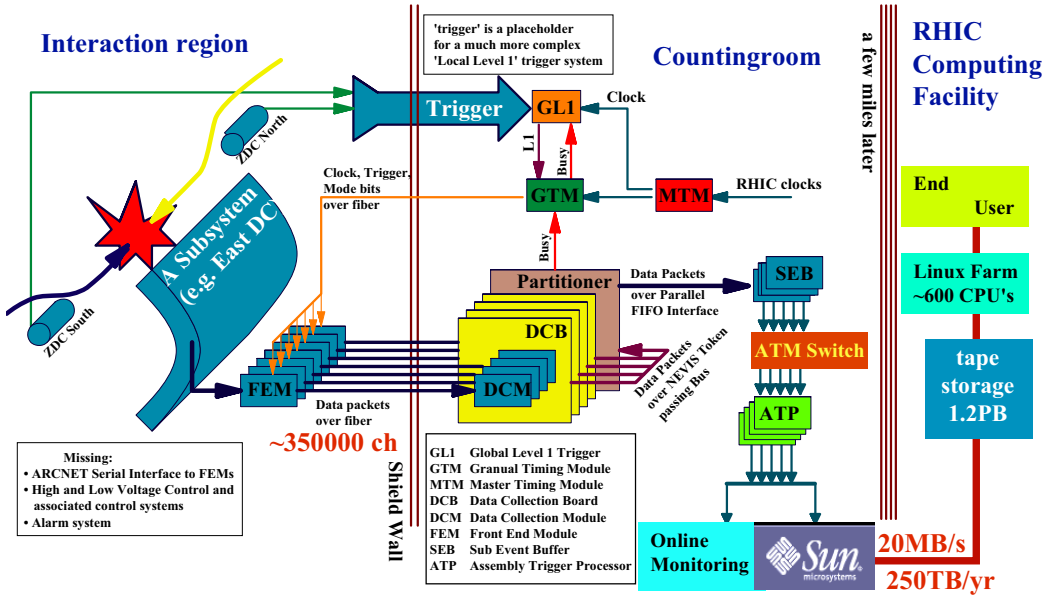


Figure 3.11: PHENIX data acquisition system.

Once an event is accepted, the Data Collection Modules (DCM) receive data via fiber-optic links from the FEM's. The DCM's perform zero suppression, error checking and data reformatting. The reformatted data packets then go to the Event Builders (EvB) that assemble the events in final format. At this stage, a level-2 trigger (LVL2) can be operated on the full event data to make finer physics event selections.

The final collected data are recorded in a form of PHENIX Raw Data Format files (PRDFs). Small data samples from the EvB are sent to the PHENIX Online Control System (ONCS) for monitoring purposes. The main data are stored in a local data disk array first and then transferred to magnetic tape in the RHIC Computing Facility (RCF)

High Performance Storage System (HPSS).

## 3.8 Offline Data Reconstruction

### 3.8.1 The PHENIX Data Flow

The data can be retrieved for HPSS for offline reconstruction. The offline data reconstruction flow consists of several steps. First, the raw output from the detectors is calibrated and converted to physics quantities such as time of flight, energy deposit, etc. In general, this only needs to be done once. Second, the PHENIX offline reconstruction software packages are used to look for particle hits and tracks in the data. The output is in the form of a Data Summary Tape (DST). It is roughly the same size as a PRDF and still contains some raw detector information. The next step of the reconstruction is to make the nDST (nano-DST) and/or pDST (pico-DST), which have highly reduced file size, for specific physics analysis.

The current PHENIX muon arm offline reconstruction software was developed in 2003. It is written in C++. In the following section, the detailed muon track reconstruction algorithm is presented.

### 3.8.2 Muon Arm Reconstruction

The reconstruction of muons is composed of two parts, the MuID road finding and the MuTr track reconstruction. The reconstruction begins with the road searching because the muon particle is triggered and identified by MuID Level-1 trigger. First, one dimensional roads are searched from both vertical and horizontal tubes in the MuID. Then

they are merged to form two dimensional roads. With certain selection criteria, the "golden" roads are projected from the MuID to the MuTr station 3 (closest station to the MuID) to look for associated hit cluster (stub). This process is repeated for each station in sequence to form the track candidates. The formed tracks are then fitted with a Kalman-filter function to determine the good tracks. Finally, the MuID is examined again to refine the roads from the track information.

#### 3.8.2.1 MuID Road Finding

As described in Section 3.5.2, the MuID is made of Iarocci tubes in each gap with vertical and horizontal orientation. So the first step is to find the clusters in the two-pack tubes of one orientation which all register signals in the event. The second or third gap is used as the starting gap (seed gap) due to lower hit occupancy from hadrons and soft-electrons in those two gaps than in the first gap. The hit clusters found in the seed gap are combined with the event vertex position (from BBC) to form the searching roads. [65] In case the hardware inefficiency may reduce the chance of finding roads, two search orders are performed:

- Gap2 → Gap1 → Gap3 → Gap4 → Gap5
- Gap3 → Gap2 → Gap1 → Gap4 → Gap5

The roads are projected from one gap to another to look for the associated hits within the search window. The window is defined as the circular area of 15 cm radius (roughly two tube widths) from the intersection of projected lines to the next gap. The hits in the search window are found and combined with the road to form extended roads. A road with no hit

in this gap is also kept. The procedures are then repeated for each gap in the search order mentioned above. A good MuID road must meet the following search criteria [66]:

- The number of hits beyond the second gap $\geq 1$.
- The number of gaps in the road $\geq 2$
- The maxima skipped gap $\leq 1$

Once the searching in the separated orientation is done, the roads from vertical and horizontal orientations are then combined into two dimensional roads. Large numbers of false roads are removed based on the following criteria:

- The depth of the roads can differ by no more than one gap.
- The number of hits in the roads can differ by a maxima of one.
- The roads from opposite orientations should transit the same panel.

In each event, there could be several similar reconstructed MuID roads which result in the similar associated tracks in the MuTr. In order to reduce the computation time of reconstructing the real track, the roads are grouped. A road is checked if it belongs to a group by:

- The hits of the road are within the window of hits from other roads.
- The projection of the road to the MuTr lies in the window of projection of other roads.

Only one road from each group is passed on to the MuTr reconstruction. The road which has the station 3 projection closest to the median of all station 3 road projections is used to represent the group.

#### 3.8.2.2 MuTr Track Fitting

The track reconstruction in MuTr starts with finding and fitting the clusters. Each MuTr chamber (station) is comprised of two or three gaps, each of which has one anode plane and two cathode planes as described in Section 3.5.1. When a charged particle passes through the chamber, it will induce charge on several consecutive cathode strips. A group of hit strips is called a cluster. The charge distribution in the cluster is then fitted with single Mathieson function[67] as shown in Figure 3.12 to obtain the charge peak position. In high multiplicity Au+Au collisions, it can happen that more than one particle hits the same strips. Thus, the charge distribution in the cluster can be fitted with a sum of two Mathieson functions if the overlap is not too large. The desired MuTr chamber plane resolution is about 100 $\mu m$ which depends on the detector geometries, noise levels and other things (like the incident angle of particles). [68] With this resolution, the expected mass resolution of $J/\psi$ is about 110 MeV. However, the actual noise level and gain fluctuation in the data are worse than the desired condition which degrades the resolution.

As mentioned in the previous section, roads from the MuID are used as seeds to search for the associated tracks in the MuTr. Hits which fall within a mask window (as shown in Table 3.2) of the projected road-station intersection are searched in last plane of MuTr station 3. When the associated hit is found, the induced clusters are grouped into a track stub in each station. For example, station 3 has two layers of anode wires and four corresponding cathode planes, so an ideal station 3 stub will be made of from four clusters, one from each cathode plane. In each station, a cluster requires at least two cathode planes to be hit. The stub provides a momentum measurement which then allows

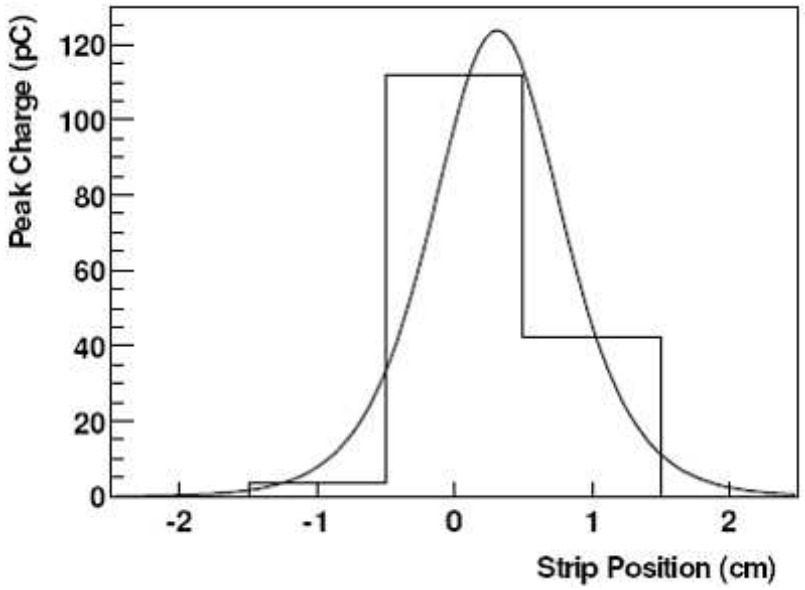


Figure 3.12: Charge distribution on cathode strips with fit to a Mathieson function.

projection through the magnetic field back to station 2.

When the stubs in station 3 are found, they are fitted to a straight line which includes the vertex point and the MuID roads. The stubs with too high $\chi^2$ are rejected. Then the qualified stubs are projected in sequence through station 2 and station 1 by using an effective bend-plane fit and momentum kick, which are determined by the approximate muon momentum and the MuTr magnetic field. The stubs associated with the real tracks in each station are searched by the window related to the projected tracks. Table 3.2 shows the search window from both the $\theta$ and $\phi$ direction at each station. The search window in station 3 is large compared to the position resolution of the MuID roads. It will become smaller when the tracks are projected through the MuTr station due to the increase of momentum resolution that can be measured.

Table 3.2: Search window definition of MuTr stations

| MuTr station | $\theta$ (cm) | $\phi$ (cm) |
|---|---|---|
| 1 | 20 | 10 |
| 2 | 30 | 25 |
| 3 | 50 | 40 |

When full tracks have been found in the MuTr, a fast fit is applied to each track by using the bend plane technique to make rough measurements of the momentum. A ghost rejection module is called which groups tracks into sets which share at least one hit in the MuTr. [69] From each set, an attempt is made to select the "best" track based on the $\chi^2$ of the track fit and the number of hits on the track. All other tracks in the set are tagged as ghost tracks. All ghost tracks are removed from the final analysis.

Once the ghost rejection is performed, a full Kalman filter fit[70] is applied to the track, to have a precise measurement of its position and momentum. The fit includes only the hits in the muon tracker and ignores the MuID road due to the poor resolution of roads in MuID at this stage. Since a large amount of absorber is present between the MuTr and the vertex, estimates for energy loss and multiple scattering have also been included.

#### 3.8.2.3 Muon Track Determination

In the first pass road finder, the reconstruction algorithm is designed to add hits to a road at the cost of missing some true hits. This helps to point accurately the roads to the MuTr. When MuTr tracks are reconstructed, the information is passed to MuID and utilized to refine the MuID roads. The second pass road finder attempts to pick up any missed true hits. Each road is projected through the entire MuID and hits which fall

within the search window for each gap are added to the road. These roads are refit, and they become the final version of the MuID roads.

A maximum of three roads can be selected to match a given track, depending on the last MuID gap they reach.

- One shallow road which reaches gap 3.
- One sheep road which reaches gap 4.
- One deep road which reaches gap 5.

They must match a given track in MuTr and pass track-road match criteria.

- The match of the position of MuTr track projected to the MuID to the MuID road position (DG0).
- The match of the slope of the MuTr track and the MuID road (DDG0).

The selection of the best road amongst these 3 candidates of different depths is left to the final part of the reconstruction chain. Fig. 3.13 shows the typical track-road match distributions from proton+proton collision data.

Once a Muon Arm track has been determined, the muon identification software also attempts to determine whether or not the particle that created the track was a muon by using the characteristics of the track:

- The magnitude of the track's momentum.
- The last MuID plane the track reaches.
- The maximum number of hits in a single MuID plane.

In addition to adding knowledge on the collision position to the track information, a vertex fit to the single track and two muon tracks is also performed. [69]

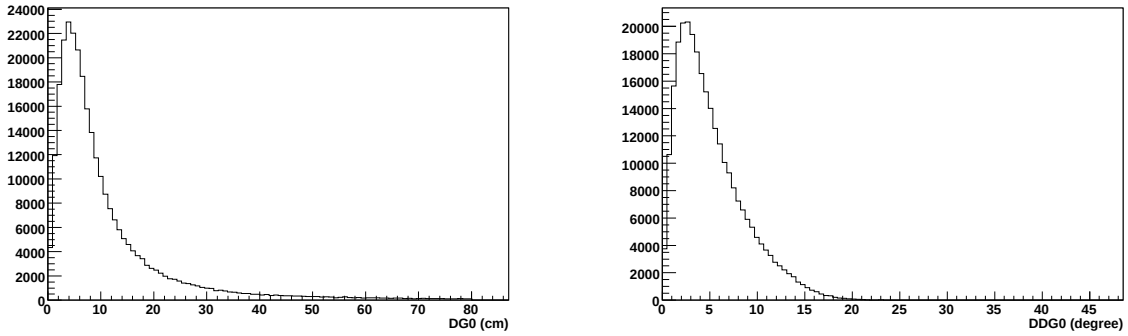


Figure 3.13: The DG0 and DDG0 distributions from proton+proton data.

# Chapter 4

# Data Analysis

As described in Section 2.3.1, the calculation of polarization parameter is done by fitting the decay dimuon angular distribution with the function of $1 + \lambda \cos^2 \theta$. The angular distribution can be measured with PHENIX Muon Arms in the muon pair decay channel. In this chapter, the PHENIX Muon Arm data from 200 GeV proton+proton collisions were analyzed to extract the $J/\psi$ polarization parameter.

## 4.1 Run5 Proton+Proton Data Set

### 4.1.1 Data Taking Summary

The PHENIX Run5 proton+proton data were collected from April 7 to June 24, 2005. It consists of $12.6pb^{-1}$ longitudinal polarized and $160nb^{-1}$ transverse polarized proton+proton data. This is the first data set available to study the $J/\psi$ polarization in a proton+proton collision system with reasonable statistics. There were three MuID Local Level-1 (LL1) triggers enabled beside the requirement of the BBC LL1 trigger. The 1D (1S)

triggers require that at least one deep (shallow) road is found in the designated MuID arm and the 1D1S trigger requires that there be at least one deep and one shallow road found in the designated MuID arm. These MuID LL1 triggers helped to accumulate rare events (e.g. $J/\psi$). After all the data were collected, it was discovered that a trigger fiber for two MuID High voltage chains had been swapped in the last gap of the North arm. This resulted in an additional inefficiency in the affected area for the MuID 1D and 1D1S triggers[71]. The MuID LL1 trigger emulator had been implemented in the muon offline analysis software to account for that effect. However, the trigger emulator was not included in the data production. The systematic uncertainty on the polarization measurement $J/\psi$ from the MuID LL1 trigger effect has been studied using simulations described in Section 4.5.4.

### 4.1.2 Data Production and Quality Assurance

A total of 260 TB (Terabytes) PRDF (PHENIX Raw Data Format) data files were transferred to and reconstructed at CCJ (Japan) with offline reconstruction library version pro.73 [72]. This resulted in 426 GB (Gigabytes) nDST (nano data summary tape) files. Then the dimuon pDST (picoDST) are produced using the MWGpico (Muon Working Group pico) software package. Certain criteria have been chosen to make good data selection [73]. The selected runs used for this analysis are listed in Appendix B.

### 4.1.3 $J/\psi$ Signal Extraction

The dimuon pDST files contain reconstructed muon track candidates (decays from $J/\psi \to \mu^+\mu^-$) in each event. In Table 4.1, the cuts used for selecting the good muon tracks and pairs are listed. The definition of the cuts is listed below:

Table 4.1: Muon track and pair selection cuts.

| | |
|---|---|
| BBC_z vertex | -30 cm < z < 30 cm |
| Invariant mass | 2.6 GeV < mass < 3.6 GeV |
| Rapidity North | 1.2 < y < 2.2 |
| Rapidity South | -2.2 < y < -1.2 |
| DG0 North | < 15 cm |
| DG0 South | < 20 cm |
| DDG0 North | < 9 degree |
| DDG0 South | < 9 degree |
| P_z North | > 0 |
| P_z South | < 0 |
| MuID Hits | 8 < hits < 10 |
| MuID Depth | 4 |
| Trk $\chi^2$ North | < 30 |
| Trk $\chi^2$ South | < 30 |
| Vertex $\chi^2$ | 4 |

- BBC_z vertex: The z vertex cut of the event collision as determined by the BBC detector.

- Invariant mass: The invariant mass window of muon track.

- Rapidity: The forward and backward geometric acceptance of the Muon Arm detectors.

- DG0: The distance of the MuTr track projected to the MuID to the MuID road position in the first MuID gap. The unit is centimeters.

- DDG0: The slope match of MuTr track (at MuTr station 3) and the MuID road (at the first MuID gap). The unit is degrees.

- MuID Hits: The number of hits in the MuID for each muon track.

- MuID Depth: The last MuID gap that the MuID road can reach. The depth of 4

means the road will reach the gap 4, which corresponds to the deep road. (When the muon reaches gap 3, the road is called sheep road and it is called shallow road when it reaches gap 2. )

- Trk $\chi^2$: The $\chi^2$ of Kalman fit on the muon track in order to reduce the background.
- vertex $\chi^2$: The approach of a dimuon pair to the BBC z vertex.

The like-sign subtraction method is used in this analysis to remove the background from the signal. For example, the background of the decay dimuon, invariant mass distribution is calculated as two times the square root of the product of plus-plus dimuon pairs and minus-minus dimuon pair in each bin.

In Fig. 4.1, the invariant mass spectra of background subtracted decay dimuons are shown. A fit function composed of a double Gaussian and exponential functions is used to fit the invariant mass spectra as shown in Fig. 4.1. The parameters of the fit function are listed as bellow.

- Fit range: 1.7-7.0 GeV
- Fit parameter(0): The initial number of $J/\Psi$ in each bin is 100.
- Fit parameter(1): The mean invariant mass is fixed at 3.12 GeV.
- Fit parameter(2): The first Gaussian width is fixed at 0.145748 (South) and 0.139726 (North).
- Fit parameter(3): The fraction of the second Gaussian to the first is fixed at 0.299087 (South) and 0.281082 (North).

- Fit parameter(4): The second Gaussian width is fixed at 0.351497 (South) or 0.399543 (North).

- Fit parameter(5): The initial exponential normalization factor is defined as the average of bins 21-25 of the subtracted mass distribution.

- Fit parameter(6): The initial exponential slope is 0.7.

The total number of $J/\psi$ signals in the mass window [2.6, 3.6] (GeV) is 4163 for the North arm and 5864 for the South arm.

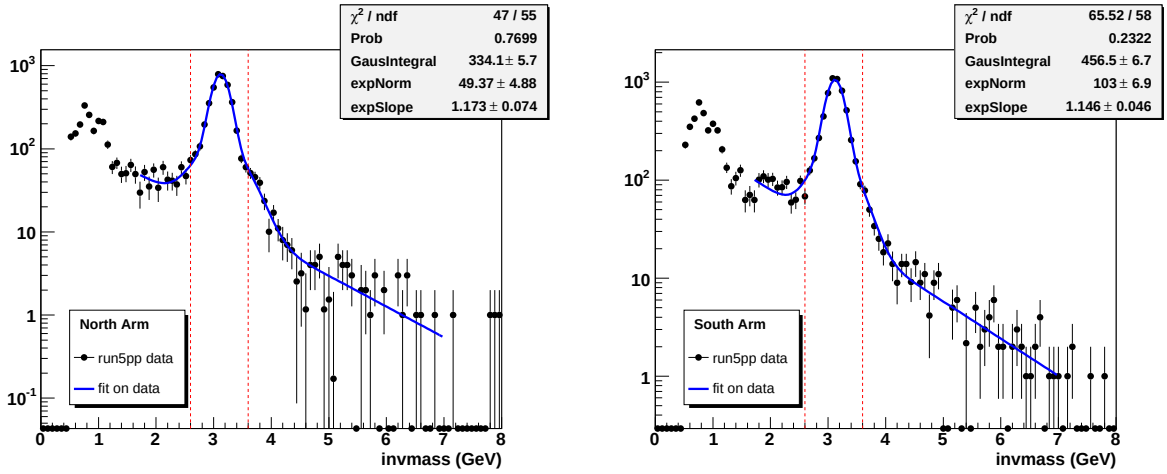


Figure 4.1: (color online) Invariant mass spectra of the data. The blue line is the invariant mass fit of data. (The dashed vertical lines show the mass cuts between 2.6 GeV and 3.6 GeV.)

The raw $\cos\theta$ distributions of the Run5, proton+proton data are shown in Fig. 4.2 together with the like-sign backgrounds. It is clear that the background is low in proton+proton data. The kinematics coverage ($p_T$ and $x_f$) and their correlation are shown in Fig. 4.3.

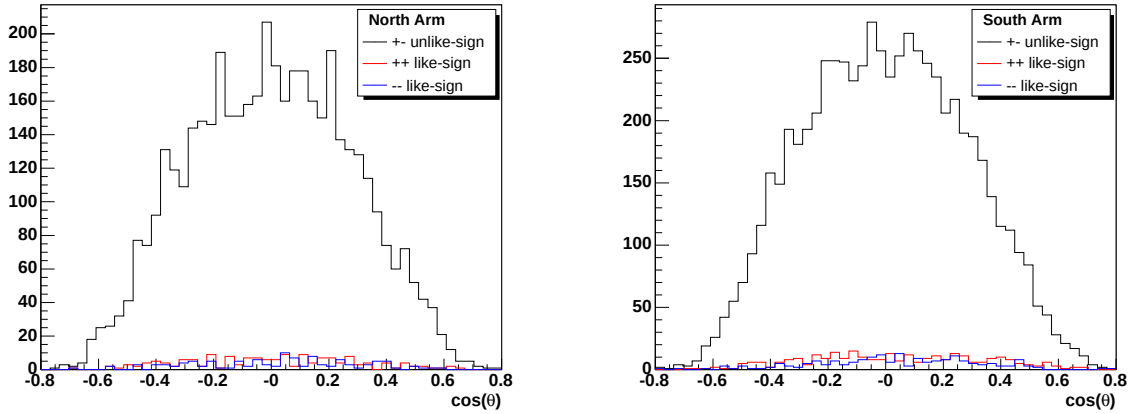


Figure 4.2: (color online) Raw $\cos\theta$ distributions from data for Muon Arms. The like-sign background is included for each arm.

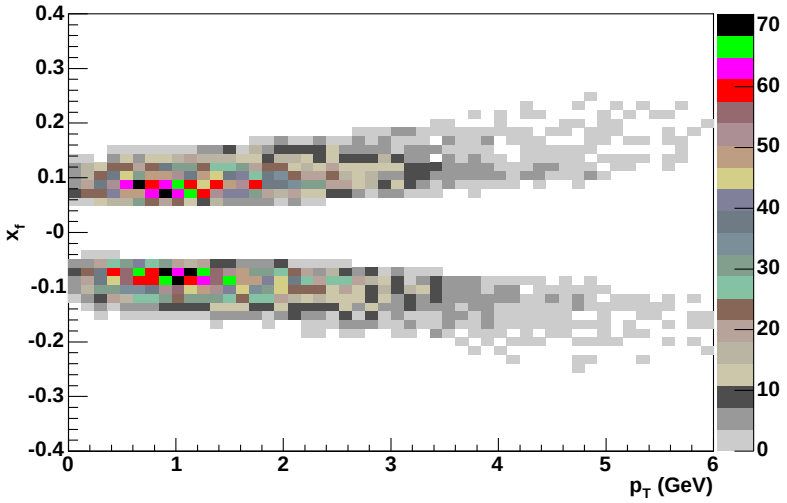


Figure 4.3: (color online) $p_T$ and $x_f$ correlation from data.

## 4.2 $J/\psi$ Acceptance in Muon Arm Detectors

To extract properly the $J/\psi$ angular distribution, we need to understand fully the acceptance of $J/\psi$ particles in the Muon Arm detectors. Monte Carlo simulation is a standard technique for calculating the acceptance of detectors. An extensive study has been done to look at the $J/\psi$ acceptance and its decay muon angular distribution ($\cos\theta$) in the PHENIX Muon Arms. The $J/\psi$ events are generated from a pure Monte-Carlo event generator with flat $p_T$, $x_f$, $\cos\theta$ and vertex distributions. Then the PHENIX simulation package PISA (PHENIX Integrated Simulation Package) [74] is used to simulate the muon tracks passing through the Muon Arms. The output from the PISA simulation is then processed through the standard PHENIX offline analysis chain. The results are given in the following subsections.

### 4.2.1 $p_T$ and $x_f$ Acceptance Distribution

Figure 4.4 shows the $p_T$ and $x_f$ acceptances of $J/\psi$ in the PHENIX Muon Arms. As shown in the figure, the $J/\psi$ acceptance increases as $p_T$ increases. However, the $x_f$ distribution is quite limited to the range of $0.05 < |x_f| < 0.25$.

### 4.2.2 $\cos\theta$ Acceptance Distribution

The $\cos\theta$ distribution in the PHENIX Muon Arms is plotted in Fig. 4.5. It shows a dramatically reduced acceptance in the large $|\cos\theta|$ region. This limited acceptance means one has to make very accurate acceptance corrections in order to extract the polarization parameter. [42]

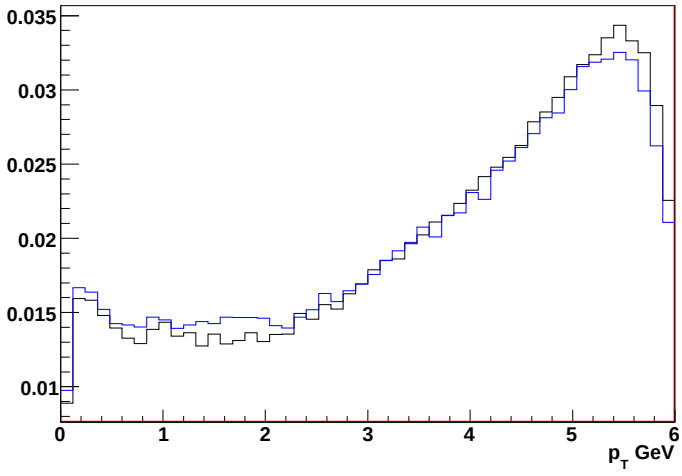


(a) (color online) $J/\psi$ $p_T$ acceptance (Blue: North, Black:South)

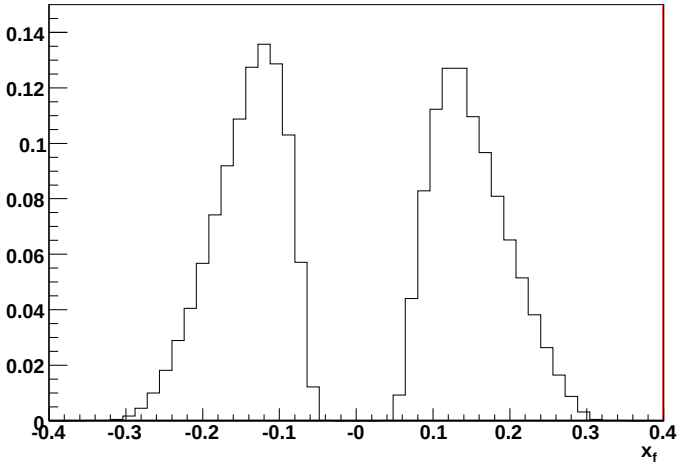


(b) $J/\psi$ $x_f$ acceptance

Figure 4.4: $J/\psi$ acceptance of $p_T$ and $x_f$ in the PHENIX Muon Arms.

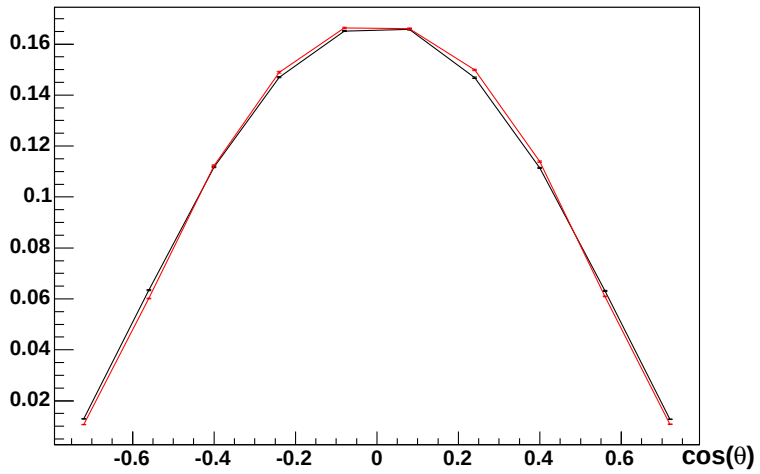


Figure 4.5: (color online) $\cos\theta$ acceptance in the PHENIX Muon Arms. (Red for the south arm, blue for the north arm.)

### 4.2.3 $p_T$ and $\cos\theta$ Acceptance Correlation

The $\cos\theta$ acceptance in the PHENIX Muon Arms is highly dependent on $J/\psi$ kinematics. As it is clearly shown in Fig. 4.6, in the low $p_T$ region, $\cos\theta$ barely goes beyond 0.6. As $p_T$ increases, the $\cos\theta$ acceptance extends to 0.8 from our simulated events. However, there are few events in the data which have $p_T$ higher than 5 GeV as shown in Fig. 4.7.

### 4.2.4 $x_f$ and $\cos\theta$ Acceptance Correlation

From the simulation, it is also clear that the $\cos\theta$ acceptance is dependent on the $J/\psi$ $x_f$ as shown in Fig. 4.8. We see that $\cos\theta$ barely goes beyond 0.6 when $|x_f| < 0.15$. From the data, there are very few events with $|\,x_f\,|$ beyond 0.2, as shown in Fig. 4.9.

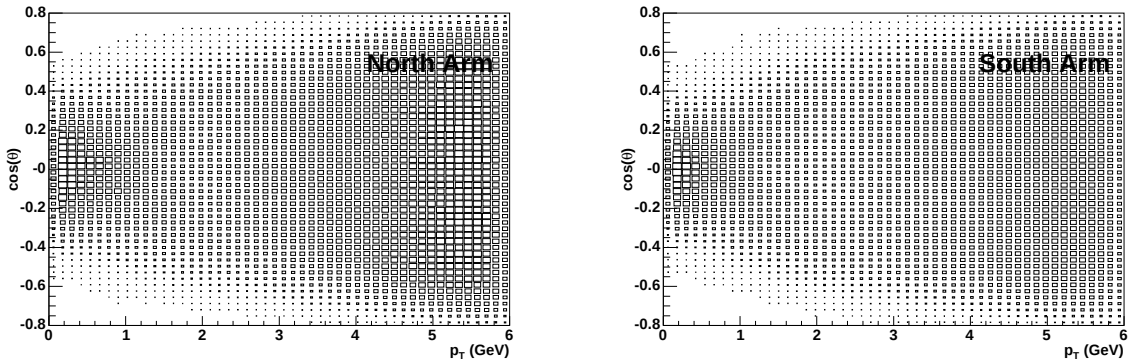


Figure 4.6: Acceptance correlation between $\cos\theta$ and the $J/\psi$ $p_T$ of simulation. In the simulation, the $J/\psi$ is generated with flat kinematic input.

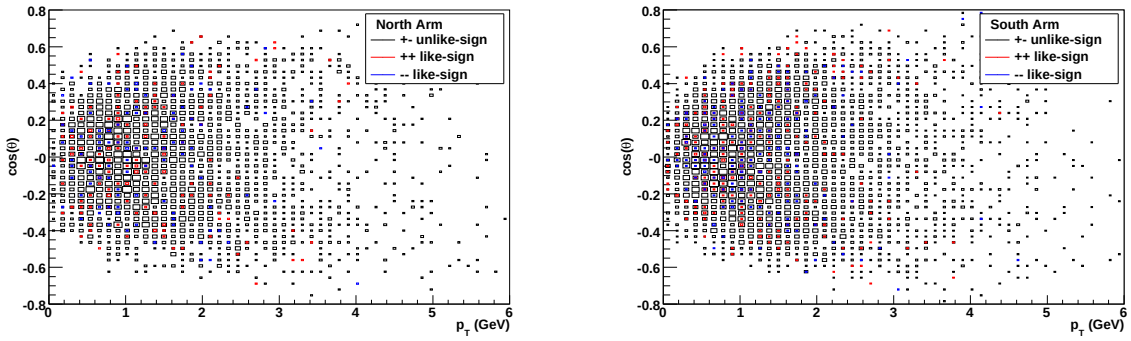


Figure 4.7: (color online) Acceptance correlation between $\cos\theta$ and the $J/\psi$ $p_T$ of data.

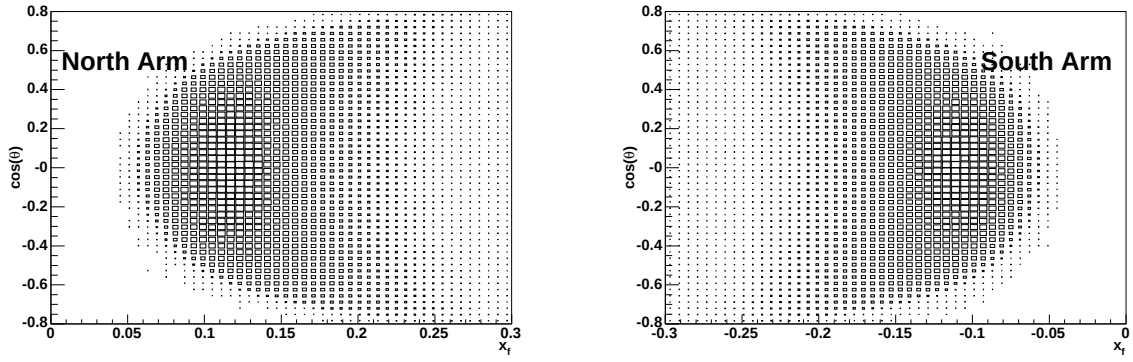


Figure 4.8: Acceptance correlation between $\cos\theta$ and the $J/\psi$ $x_f$ of simulation. In the simulation, the $J/\psi$ is generated with flat kinematic input.

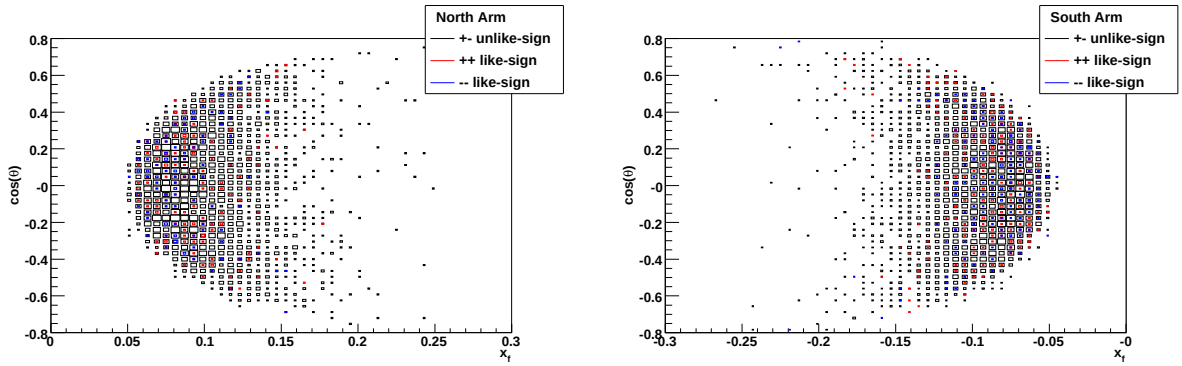


Figure 4.9: (color online) Acceptance correlation between $\cos\theta$ and the $J/\psi$ $p_T$ of data.

### 4.2.5 Vertex and $\cos\theta$ Acceptance Correlation

In the PHENIX experiment, valid collision vertex positions vary from -30 cm to +30 cm relative to the geometric center of the PHENIX detector system. In order to look at the vertex dependence of the $\cos\theta$ acceptance, 250k events were generated within each of the following vertex windows

$$[-30cm, -15cm],\ [-15cm, -5.0cm],\ [-5.0cm, 5.0cm],\ [5.0cm, 15cm],\ [15cm, 30cm].$$

Figure 4.10 shows the $\cos\theta$ acceptances for those vertex regions. The vertex influence on the $\cos\theta$ acceptance within the PHENIX Muon Arms is demonstrated by taking the ratio between the accepted $\cos\theta$ distribution at the $(\pm 30cm)$ vertex position and the distribution at the vertex zero position. This ratio is given in Fig. 4.11. The vertex effects get larger near the limits of the $\cos\theta$ acceptance.

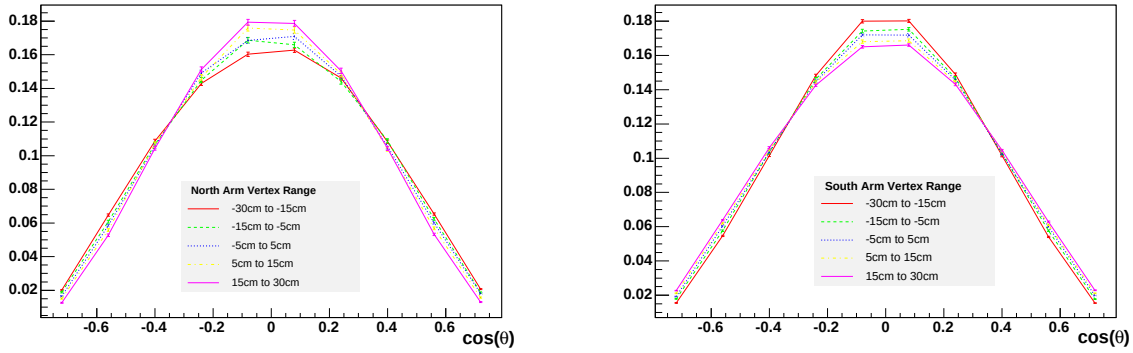


(a) North Arm (b) South Arm

Figure 4.10: (color online) The $J/\psi$ acceptance at different vertex positions.

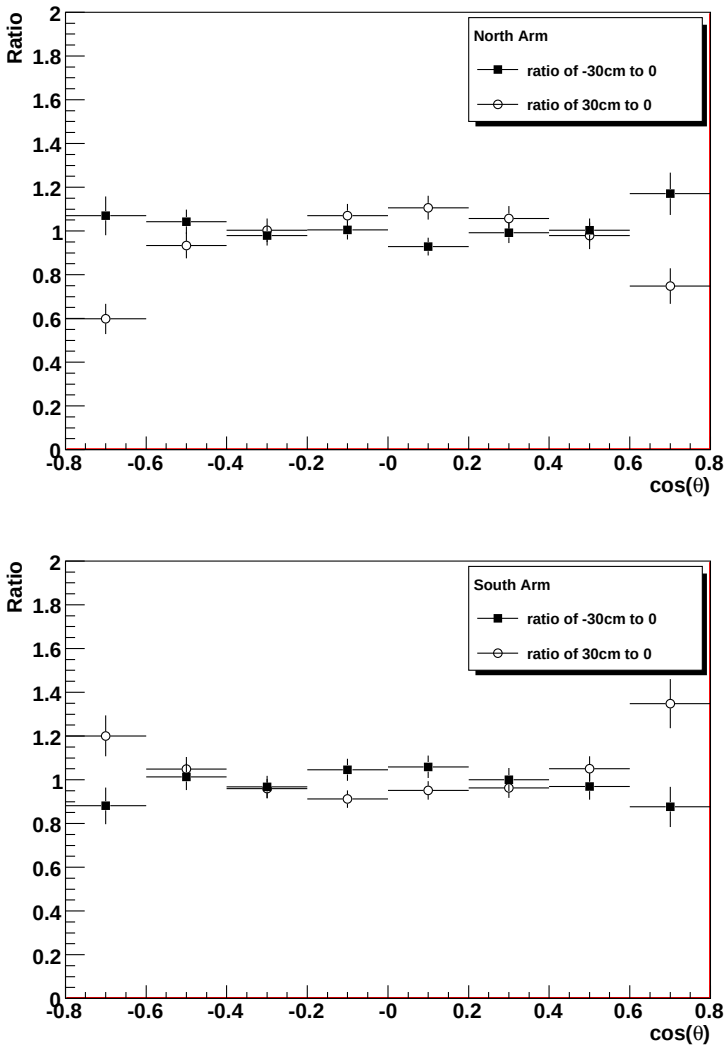


Figure 4.11: The ratio of the $\cos\theta$ acceptances between the two vertex regions.

## 4.3 Trigger and Muon Arm Detector Efficiency

### 4.3.1 Muon Trigger Effects on $\cos\theta$ Acceptance

Run5 proton+proton data from the Muon Arms were taken with the online MuID LL1 triggers enabled. [75] After the data were saved on disks in the PHENIX counting house, a second level filtering process was applied to the data to further condense the $J/\psi$ event sample for a fast offline physics analysis. So it is important to check out the triggering effects on the $\cos\theta$ distribution and correct the effects properly.

First, the Lvl1 triggering effect is studied in simulations where an offline 1D1S LL1 emulator was enabled. This trigger requires at least 1 deep ( MuID road reaches gap 4) and 1 shallow ( MuID road reaches gap 2 and 3) trigger in each event. Second, a L2dimuon_ok cut in the simulation is used for studying the Lvl2-filtering effect on $\cos\theta$. It requires that the MuID number of roads in each event is $\geq 2$, the penetration depth of each road is to gap4 (last gap), the slope of the two deep roads is $\geq 12$ degrees, the opening angle between two MuID roads is $\geq 19.2$ degrees and the number of hits per road is $\geq 8$.

The trigger effects on $\cos\theta$ distributions are plotted in Fig. 4.12. One of the ratios shown in the figure is taken between the case with the MuID 1D1S LL11 emulator enabled and the case without LL1 triggering. The other ratio is between the case with the MuID 1D1S LL11 emulator enabled together with the L2dimuon_ok cut, and the case without any triggering selection.

It shows that when the triggers are applied, more events will be accepted in the small $\cos\theta$ region and fewer events will be accepted in the large $\cos\theta$. Moreover, the effect from the Lvl2 trigger is slightly larger than the effect from LL1 trigger, especially in the large

$\cos\theta$ region. Since only the LL1 triggered data were used for this analysis, the Lvl2-filtering effect is not considered in this analysis.

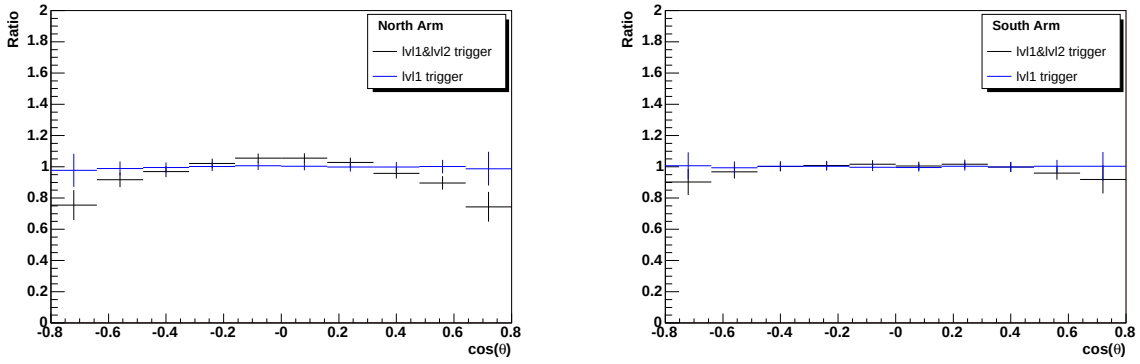


Figure 4.12: (color online) The ratio of $\cos\theta$ with muon trigger cuts to $\cos\theta$ without cuts.

### 4.3.2 MuTr Detector Efficiency Dependence of $\cos\theta$

The efficiency variation of MuTr can affect the $\cos\theta$ distribution. The MuTr high voltage (HV) performance during the data taking period has been reviewed to study the effects. Figure 4.13 shows the number of bad/disabled HV channels as a function of the run number. This run-by-run HV performance variation is used to define the run groups for studying the MuTr efficiency performance. Note that 48 HV channels in the south arm, which are the inner anodes and lie in front of the piston at 10-12 degrees, were purposefully turned off during the run. This made the variation of real dead channels range from 2 to 8 as shown in Fig. 4.13 (b). For the north arm, the MuTr bad/disabled HV channels vary between 10 to 14.

Based on the HV variation discussed above, four sets of simulations were done in

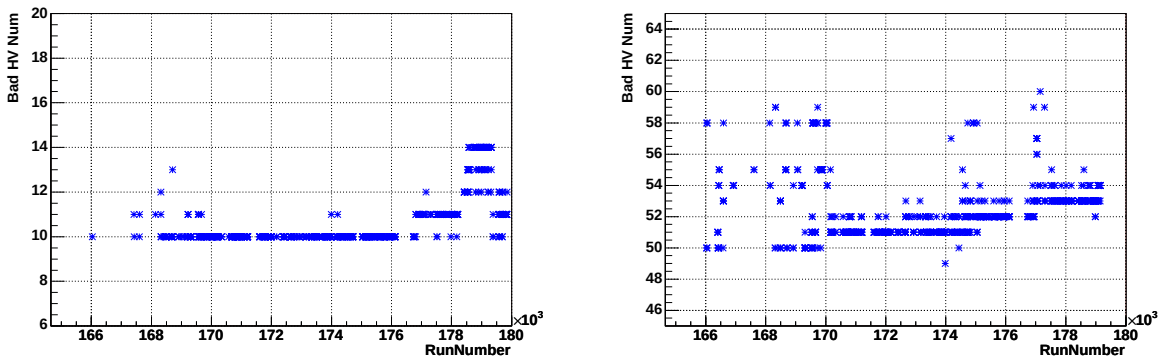


(a) North Arm (b) South Arm

Figure 4.13: Number of Muon Tracker bad/disabled HV channels versus run number.

order to characterize the HV effects on the $\cos\theta$ acceptance with the following configurations:

- 10 bad/disabled channels for the north arm
- 14 bad/disabled channels for the north arm
- 50 bad/disabled channels for the south arm
- 58 bad/disabled channels for the south arm

In Fig. 4.14(a), a ratio of the $\cos\theta$ distributions is plotted for the north arm between the first HV configuration and the second. Figure 4.14(b) shows the the same ratio between the third configuration and the fourth. It is observed that the effect of the bad/disabled MuTr HV channels on the $\cos\theta$ distribution is quite small overall.

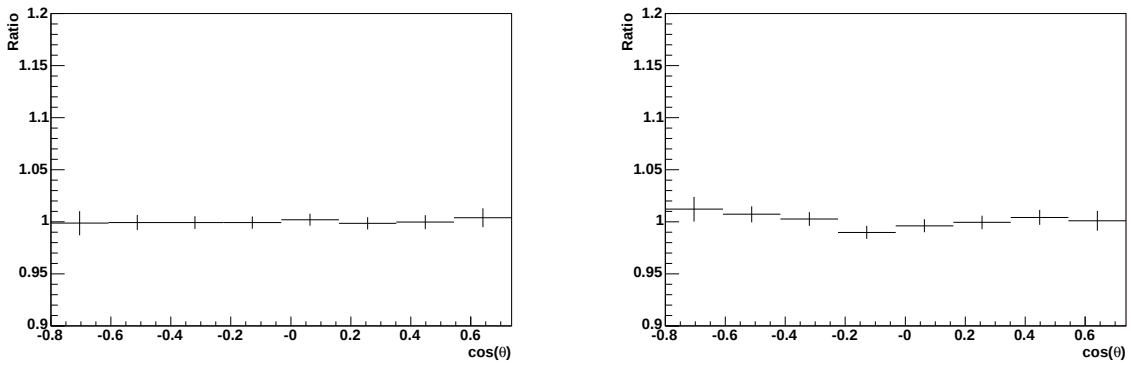


(a) North Arm (b) South Arm

Figure 4.14: The MuTr HV effects on $\cos\theta$ acceptance. The ratio of the $\cos\theta$ distributions from two HV configurations as described in the text.

### 4.3.3 MuID Detector Efficiency Dependence of $\cos\theta$

The effect of the MuID efficiency on the $\cos\theta$ distribution has also been analyzed with simulations. The nominal MuID tube efficiency which is used for this analysis is described in the PHENIX analysis note 598 [73]. Two sets of simulations were run: The first is with the nominal tube efficiency configuration; and the second is with 10% reduction of all tube efficiencies relative to the nominal configuration. The 10% variation is likely the maximum for MuID. The typical tube efficiency variation is less than 5% according to our MuID experts.

Figure 4.15 shows the ratio of the $\cos\theta$ distributions between the two sets of simulations. Although there is a slight deviation from 1 in the large $\cos\theta$ regions, no significant effect is observed from the MuID tube inefficiencies. This variation is, indeed, included in our estimation for the overall systematic error of the extracted $J/\psi$ polarization

result.

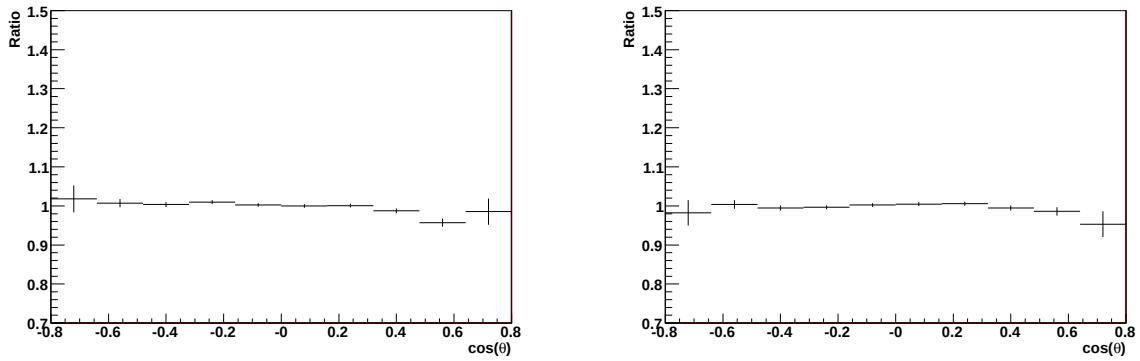


(a) North Arm (b) South Arm

Figure 4.15: The MuID tube efficiency effect on the $\cos\theta$ distribution. The ratio is taken with $\cos\theta$ in 10% reduced MuID tube efficiency to the nominal efficiency from simulation.

#### 4.3.3.1 Reference Run Dependence

In order to check the reference run dependency of the $\cos\theta$ distribution, two reference runs (run 175777 and run 179571) were selected for running simulations. The run 175777 is roughly in the middle of the good run list and the run 179571 is close to the end of the run period. There was a short 400 GeV test run between those two runs.

The ratios of the $\cos\theta$ distributions for each muon arm from these two simulations are shown in Fig.4.16. There is no significant run-by-run variation observed. The run-by-run variation is also included in the estimation for the overall systematic error of the extracted $J/\psi$ polarization result, which is given in Section 4.5.3.

For a consistently check, a single muon yield per run has been plotted in Fig. 4.17 It shows that the muon yield is very consistent through the Run5 period.

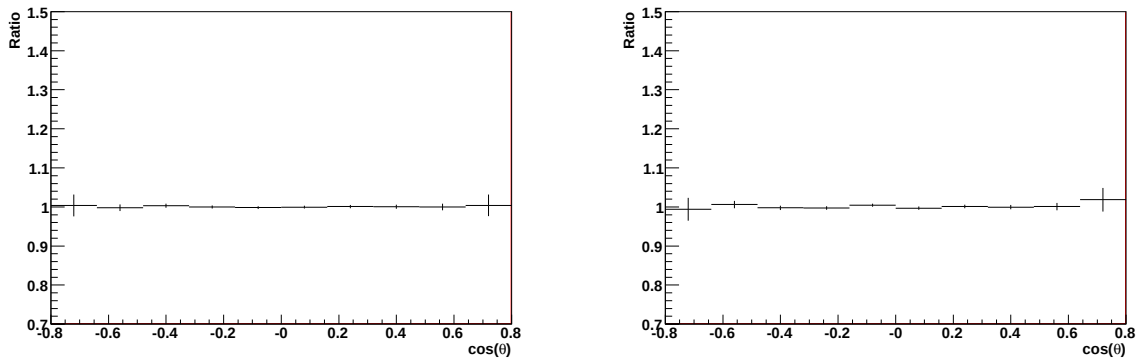


(a) North Arm (b) South Arm

Figure 4.16: The ratio of $\cos\theta$ with reference run 175777 to that with 179571.

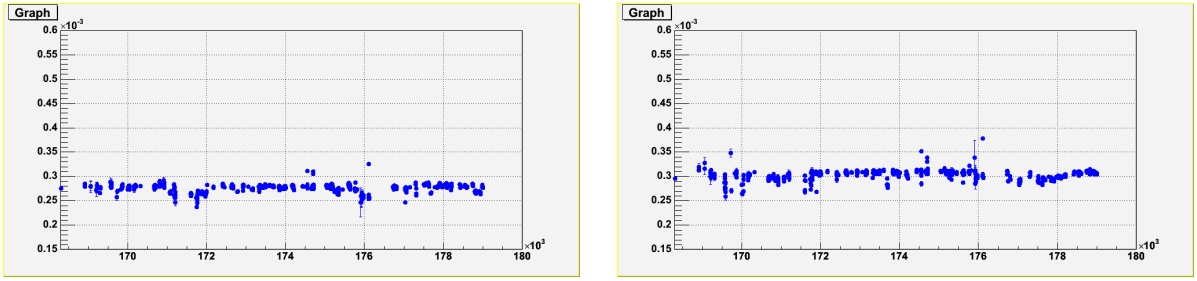


(a) North Arm (b) South Arm

Figure 4.17: Single muon yield per run versus run number.

## 4.4 Acceptance Correction Simulation

### 4.4.1 General Acceptance Correction Procedure

As it has been shown in Section 4.2, the $\cos\theta$ distribution is significantly influenced by the $J/\psi$ kinematic distributions. A two-step acceptance correction procedure has been developed for studying the polarization of $J/\psi$ in the PHENIX muon arm detectors [43].

**First step (called MC1)** In the first step, Monte Carlo events of $J/\psi$ particles with flat kinematics ($p_T$, $x_f$) and vertex inputs were generated, and these events were then run through the standard offline analysis chain for the muon arm detectors. The reconstructed $J/\psi$ distribution (with the same event selection criteria as used for the data) was then used to extract a two-dimensional correlated $J/\psi$ distribution in $p_T$ and $x_f$ from the data.

**Second step (called MC2)** In this step, the corrected $p_T$, $x_f$ and vertex distributions from the first step were then used as sample input for generating $J/\psi$ events for making the final acceptance correction for the $\cos\theta$ measurement. The same offline chain was also applied to these events. The true (i.e., measured) $\cos\theta$ distribution is the ratio between the data distribution and the $J/\psi$ distribution from this step.

### 4.4.2 Simulation Analysis Chain

Fig. 4.18 shows the simulation analysis chain for the PHENIX Muon arm. The Monte-Carlo events have been generated from flat and real (data driven) kinematic input distributions as stated previously. The purpose is to make the proper acceptance corrections for the data. However, the simulation procedure is an interactive process because the

acceptance depends on the input distribution and the distributions rely on the knowledge

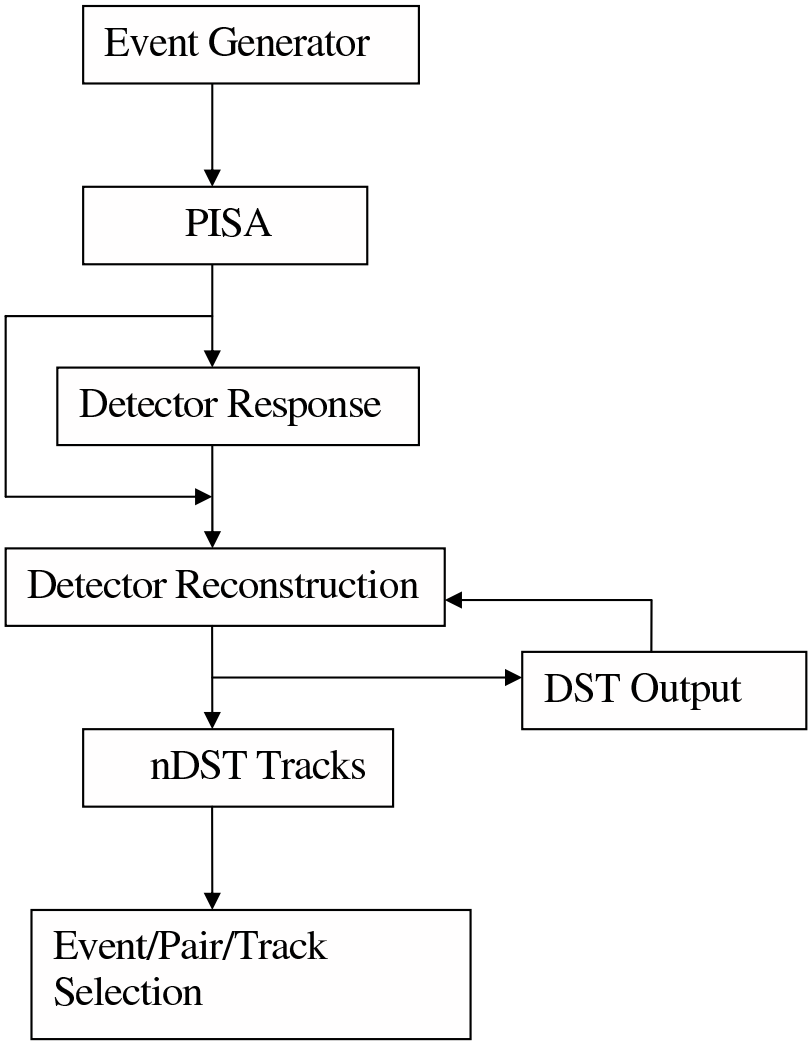


Figure 4.18: Muon arm simulation analysis chain. Note that the PISA output can be directly used for reconstruction after properly reformating unless the PHENIX raw data format is needed. Also the DST output can be resubmitted for reconstruction in case the pattern recognition is improved.

of the acceptance. We cross check the kinematics output of the second step simulation (which will be used to make final acceptance correction for data) against the real data in section 4.4.4.2.

PHENIX is a very complicated experiment which consists of a large variety of detector types and materials inside the detectors. To study the detector performance and track particles produced by the event generators, the PISA simulation package has been developed. GEANT 3.21, the Fortran language based software package, was used for generating the detector geometry and the interactions of particles with the materials of the subsystem detectors. The magnetic fields are also implemented in the PISA package. For this study, we use the 3D– magnetic field map, December 2004 version, which includes the field in the muon magnet backplates.

The output from PISA is a so-called "hits file" which contains particle identification, momenta and energy in the active detectors and the time of the particles traveling from the primary interaction vertex to the detectors. Since the PISA output already has particle hit information, it can be directly processed in the detector reconstruction step to reconstruct tracks of the signal particle. However, in order to match the real data analysis procedure or to make the embedding of signal/background available (especially for collisions with high multiplicity), the detector response step is also processed.

The Muon detectors response is simulated with the following:

- The real detector geometry was used together with the MuTr and MuID alignment offset.
- The configuration of dead/disabled high voltage (HV) channels in the MuTr is simulated, this is also true for the dead electronics and wires. The MuID chain-to-chain tube efficiencies determined from data were simulated in the Mento Carlo (MC) simulation.

- Gains and pedestals determined from real data are used to set charge spectra and noise levels for each readout channel. If zero or minimal gain is measured from real data, the channel is effectively disabled for both MC simulations and real data analysis.

- For the charge deposition in a tracker chamber, the Landau scales and offsets were set to match the real data Landau distributions.

- The value for tracker chamber efficiency is set consistent with that measured by real data.

- Zero suppression is simulated to match the real data online suppression.

After the detector response, the output is either in the format of PRDF (PHENIX Raw Data File, which has same format as the collected real data) or DST (Data Summary Tape). The reconstruction software is then used to rebuild the tracks for the simulated events. The details of Muon arm reconstruction are dscribed in Section 3.8.2.

The output from the reconstruction step is called a nano-DST file which contains the muon tracks in each event. The output can also be in the format of DST which can be stored for the next round of reconstruction where the pattern recognition software is improved. For the nano-DST output, the same event/pair/track selection cuts used for real data have been used to pick out the $J/\psi$ signals.

### 4.4.3 Simulation Setup

The simulation configurations used for this analysis are listed in Table 4.2. The muon arm offline analysis library with version 78 was used in each step of this analysis.

Table 4.2: Run5 proton+proton simulation configurations.

| | |
|---|---|
| Reconstruction lib | lib. production 78 |
| MuID South Eff | /offline/analysis/MuIDeff/results/ MuIDeff_run5_PP_200GeV_twopack_south.dat |
| MuID North Eff | /offline/analysis/MuIDeff/results/ MuIDeff_run5_PP_200GeV_twopack_north.dat |
| MuID alignment | /afs/rhic.bnl.gov/PHENIX/users/ hpereira/muons/work/pisa_to_dst/alignment_corrections.txt |
| MuTr alignment | /afs/rhic.bnl.gov/PHENIX/users/ hpereira/muons/work/pisa_to_dst/mut.internalAligConsts.dat |
| MuTr Disabled anodes | /PHENIX/data25/butsyk/run5pp/ mike/mut.disabledAnodes_run5_pp.dat |
| MuTr Disabled wires | Run Database |
| Reference run | 179571 |

### 4.4.4 Simulation Results

#### 4.4.4.1 Results from the MC1 Step

The extracted $p_T$, $x_f$ and vertex distributions from the MC1 step are shown in Figs. 4.19, 4.20 and 4.21, respectively. These distributions are used as the inputs for the MC2 step as described earlier.

#### 4.4.4.2 Results from the MC2 Step

Figure 4.22 shows the comparison between the invariant mass distributions from data and the simulations after the second step simulation. A normalization to the peak value was used for making the comparison plot. The mean value and sigma of the invariant mass fit (with a Gaussian function) from data and simulation are listed in Table 4.3.

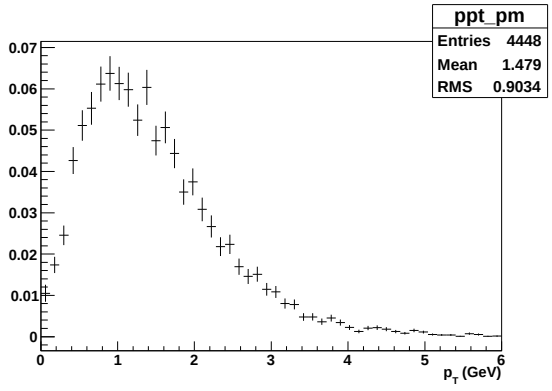


(a) North Arm

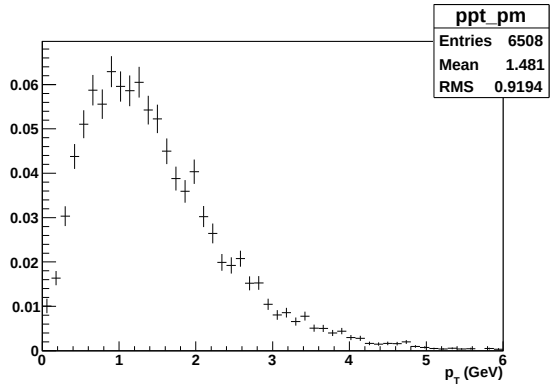


(b) South Arm

Figure 4.19: Acceptance corrected $p_T$ distribution. The distributions are normalized to 1.

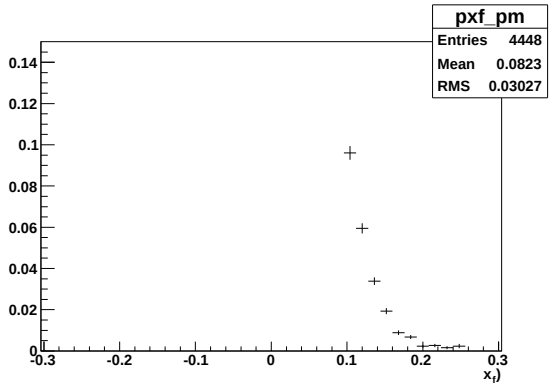


(a) North Arm

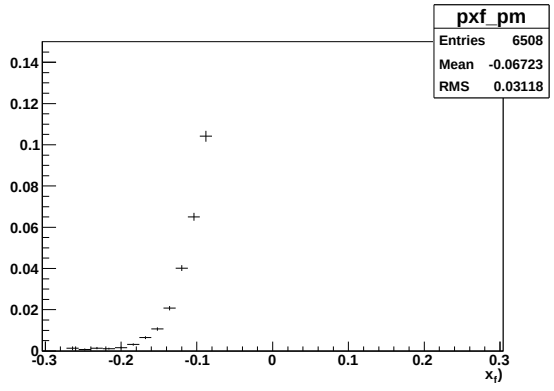


(b) South Arm

Figure 4.20: Acceptance corrected $x_f$ distribution. The distributions are normalized to 1.

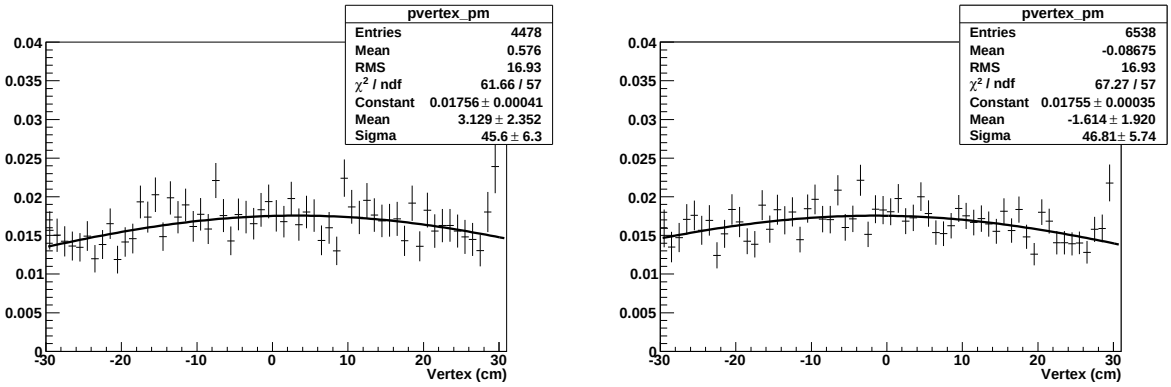


(a) North Arm (b) South Arm

Figure 4.21: Acceptance corrected vertex distribution. The distributions are normalized to 1.

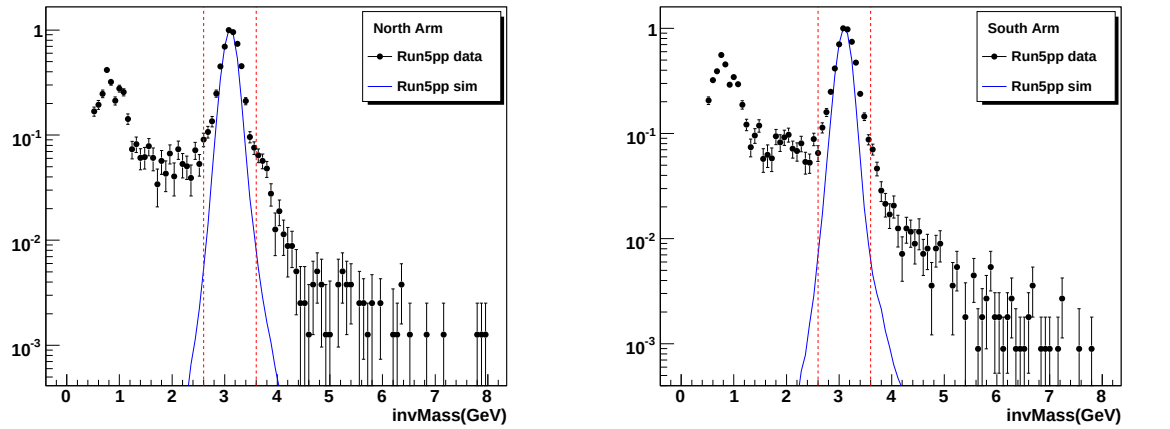


(a) North Arm (b) South Arm

Figure 4.22: Comparison of invariant mass distributions.

Table 4.3: Fit comparison between data and simulation

| Arm | North Arm | | South Arm | |
|---|---|---|---|---|
| Fit parameters | mean (GeV) | sigma (GeV) | mean (GeV) | sigma (GeV) |
| data | 3.11 | 0.185 | 3.11 | 0.196 |
| simulation | 3.10 | 0.130 | 3.11 | 0.129 |

The data and simulation are very consistent within the $J/\psi$ invariant mass window. However, the sigma from the simulation is smaller than the value from the data for both arms. For future studies, one may also want to extract a proper invariant mass distribution as a part of the inputs for the MC2 simulation.

The kinematics comparisons of data and simulation are plotted in Fig. 4.24 and 4.25, and they show very good agreement. The normalized $\cos\theta$ distribution from this step (as shown in Fig. 4.23) is used to correct the $\cos\theta$ distribution from the data. The acceptance corrected $\cos\theta$ distribution is fitted with the function $1 + \lambda cos^2\theta$ to get the measured value of the polarization parameter $\lambda$. The results are presented in Section 5.

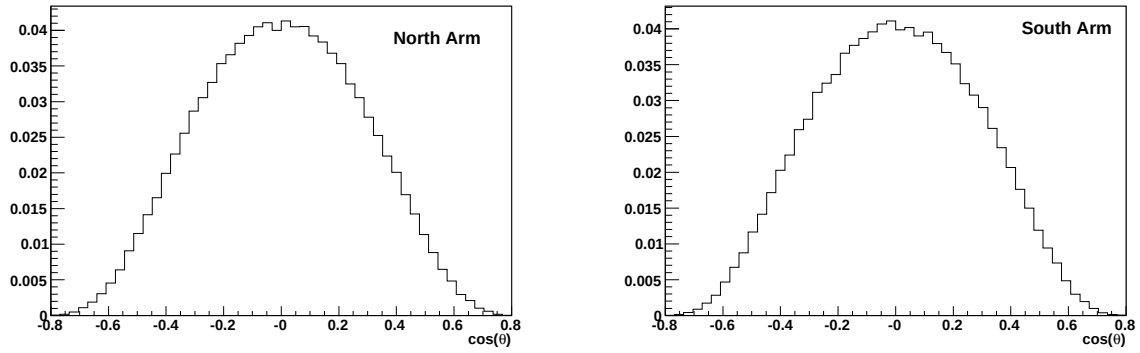


Figure 4.23: Acceptance corrections for the $\cos\theta$ distributions.

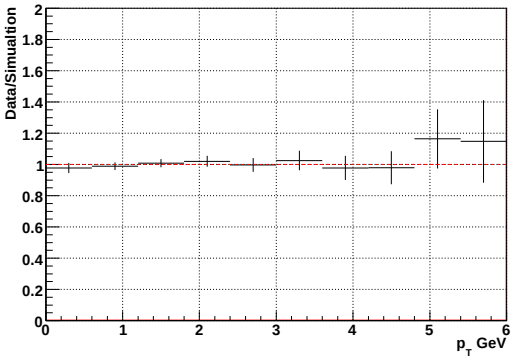


(a) North Arm

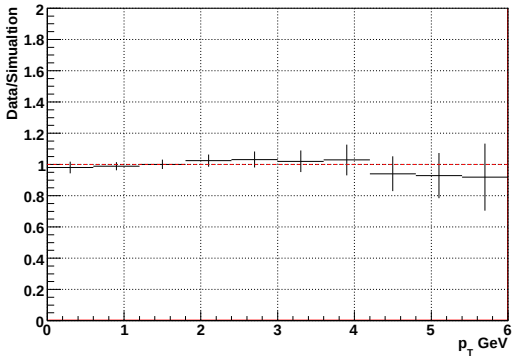


(b) South Arm

Figure 4.24: The ratio of $p_T$ distribution from data to MC1 simulation. The simulation shows a good agreement with data in $< 2\%$ when $p_T < 5GeV$ which comprises 98.7% of the data.

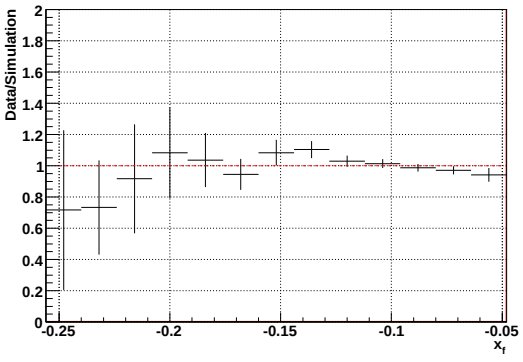


(a) North Arm

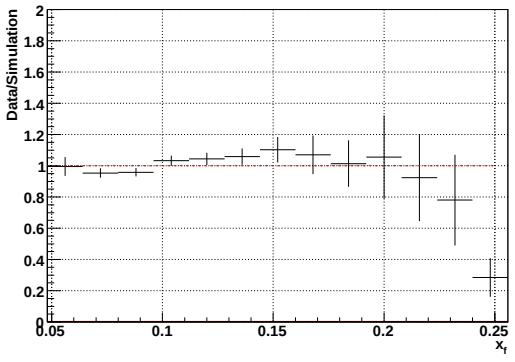


(b) South Arm

Figure 4.25: The ratio of $x_f$ distribution from data to MC1 simulation. The simulation shows a good agreement with data when $|x_f| < 0.2$ which comprises 98.8% of the data.

## 4.5 Systematic Error Analysis

The uncertainties of $J/\psi$ polarization measurement include two parts: statistical and systematic uncertainties. The statistical error comes from the data $J/\psi$ counts in the fit region and the statistics of simulation used for acceptance correction. Since the simulation has been generated with a high number of events compare to the data, the statistical error from the simulation is suppressed. The statistical error of $\lambda$ is shown in Table 5.2. In the following sections, we focus on the discussion of the systematic errors.

The sources of the systematic uncertainty of the $\cos\theta$ measurement have been partly discussed in Section 4.3. All of these error sources and the types of error are summarized in Table 4.4. The systematic errors are combined with statistical errors in making the final fit to the combined $\cos\theta$ distribution from two Muon arms for obtaining the final $J/\psi$ polarization. Different from Section 4.3, the $\cos\theta$ distributions have been re-binned into 20 bins from -1.0 to 1.0 in order to choose conveniently the bins of $\cos\theta$ and estimate properly the systematic errors. The re-binned results are consistent with the results when 10 bins are used. The detailed calculations and demonstration of the systematic errors are given in the following sections.

Table 4.4: Summary of systematic errors.

| Source | Type | Section |
|---|---|---|
| MuTR efficiency | correlated | Section 4.5.1 Ana598 |
| MuID efficiency | correlated | Section 4.5.2 Ana501 |
| run to run | correlated | Section 4.5.3 |
| Lvl1 Trigger | correlated | Section 4.5.4 |
| fit edge effect | global | Section 4.5.5 |
| data Rebin | global | Section 4.5.6 |
| data bin shift | global | Section 4.5.7 |

### 4.5.1 MuTr Detector Acceptance and Efficiency

The bin-by-bin systematic uncertainty of the $\cos\theta$ distribution, related to the MuTr detector efficiency, is calculated from the ratios in Fig. 4.14 with 20-bin binning of $\cos\theta$ from -1.0 to 1.0. In all follow sections, the error is calculated by the absolute variation of the $\cos\theta$ distributions from different simulation configurations described in Section 4.3.

Table 4.5: Systematic errors from MuTr efficiency variations.

| $\cos\theta$ bin | North Arm | South Arm |
|---|---|---|
| [-0.6, -0.5] | 0.005 | 0.03 |
| [-0.5, -0.4] | 0.004 | 0.02 |
| [-0.4, -0.3] | 0.002 | 0.004 |
| [-0.3, -0.2] | 0.007 | 0.001 |
| [-0.2, -0.1] | 0.005 | 0.005 |
| [-0.1, 0] | 0.006 | 0.01 |
| [0, 0.1] | 0.005 | 0.008 |
| [0.1, 0.2] | 0.001 | 0.003 |
| [0.2, 0.3] | 0.005 | 0.002 |
| [0.3, 0.4] | 0.001 | 0.002 |
| [0.4, 0.5] | 0.008 | 0.007 |
| [0.5, 0.6] | 0.01 | 0.015 |

There is also a consideration that the systematic error comes from the acceptance of MuTr detector. The $\phi$ angle distribution of muon tracks from data and simulation after the $J/\psi$ cuts are plotted in Figure 4.26. It's observed that the $\phi$ distribution match between the data and simulation is pretty good although the data statistics are low which makes it hard to quantify the difference at this stage.

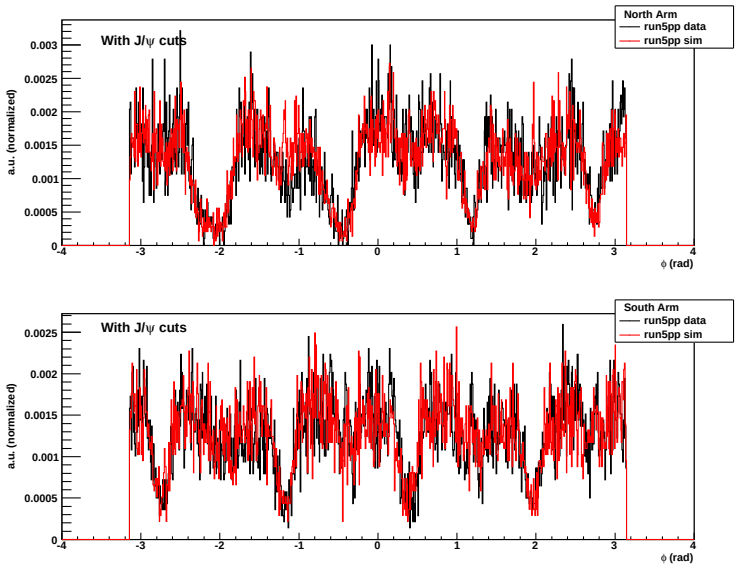


Figure 4.26: (color online) Muon tracks $\phi$ angle distribution comparison.

### 4.5.2 MuID Detector Acceptance and Efficiency

As described in Section 4.3.3, the effect of the MuID detector efficiency on the $\cos\theta$ distribution is estimated by varying the MuID tube efficiency by 10% relative to its nominal efficiency values of all tubes.

Also, as documented in the MuID analysis note 501 [76], the north arm plane 3 (gap 1 vertical), panel 4, hv group 0 was on before run 169596 and off after run 169719. This makes the MuID lose a certain area of acceptance. Simulation has been done to investigate this effect on the $\cos\theta$ distribution. Finally, the estimated bin-by-bin errors from combining the acceptance and efficiency variation of MuID is tabulated in Table 4.6.

Table 4.6: Systematic errors from MuID inefficiency variations.

| $\cos\theta$ bin | North Arm | South Arm |
|---|---|---|
| [-0.6, -0.5] | 0.056 | 0.04 |
| [-0.5, -0.4] | 0.028 | 0.02 |
| [-0.4, -0.3] | 0.011 | 0.01 |
| [-0.3, -0.2] | 0.011 | 0.007 |
| [-0.2, -0.1] | 0.010 | 0.001 |
| [-0.1, 0] | 0.003 | 0.002 |
| [0, 0.1] | 0.004 | 0.01 |
| [0.1, 0.2] | 0.005 | 0.01 |
| [0.2, 0.3] | 0.006 | 0.02 |
| [0.3, 0.4] | 0.012 | 0.01 |
| [0.4, 0.5] | 0.022 | 0.02 |
| [0.5, 0.6] | 0.036 | 0.03 |

### 4.5.3 Run to Run Variation

The bin-by-bin systematic uncertainties of the $\cos\theta$ distribution from run variations are estimated from the ratio plots in Fig. 4.16, which are given in Table 4.7.

### 4.5.4 Lvl1 Trigger Effect

The systematic uncertainties from the muon Lvl1 trigger effect on the $\cos\theta$ distribution are shown in Fig. 4.12. The bin-by-bin systematic uncertainties (in 20-bin binnings) are given in Table 4.8.

### 4.5.5 Fitting Edge Effect

Since the acceptance of the $J/\psi$ signal in the Muon Arms drops dramatically when $|\cos\theta| > 0.6$; the numerical fit for obtaining $\lambda$ is limited to the range of $-0.6$ to 0.6 in $\cos\theta$. In order to estimate the (global) systematic error caused by the fitting limit, another fit has

Table 4.7: Systematic errors from run to run variation.

| $\cos\theta$ bin | North Arm | South Arm |
|---|---|---|
| [-0.6, -0.5] | 0.004 | 0.004 |
| [-0.5, -0.4] | 0.004 | 0.004 |
| [-0.4, -0.3] | 0.002 | 0.002 |
| [-0.3, -0.2] | 0.002 | 0.003 |
| [-0.2, -0.1] | 0.002 | 0.003 |
| [-0.1, 0] | 0.001 | 0.003 |
| [0, 0.1] | 0.002 | 0.003 |
| [0.1, 0.2] | 0.003 | 0.006 |
| [0.2, 0.3] | 0.003 | 0.003 |
| [0.3, 0.4] | 0.003 | 0.002 |
| [0.4, 0.5] | 0.001 | 0.002 |
| [0.5, 0.6] | 0.003 | 0.004 |

been done to extend the fitting range from $\pm 0.6$ to $\pm 0.8$. Both of these fitting results are plotted in Fig. 4.27 together with the $\cos\theta$ data points. The fitting edge effect is calculated as the absolute value change between the two fitting functions at $\cos\theta = 0.6$, which gives the maximal global systematic error for each data point of $\cos\theta$ from the fitting edge effect. The error for the north arm is 0.0360 and 0.0504 for the south arm. The $\lambda$ values from these two fit functions are given as follows, which are statistically equivalent,

$$\lambda_{0.6} = 0.22 \pm 0.21 \quad \text{(north arm)} \qquad -0.03 \pm 0.16 \quad \text{(south arm)}$$

$$\lambda_{0.8} = 0.12 \pm 0.18 \quad \text{(north arm)} \qquad -0.18 \pm 0.14 \quad \text{(south arm)}$$

where errors are statistical only.

### 4.5.6 Data Rebin Effect

At this stage, the statistics of data are still limited. It can be observed from Fig. 4.2 that the $\cos\theta$ distribution is not smooth. Choosing different bins of $\cos\theta$ could have an

Table 4.8: Systematic errors from the Lvl1 trigger effect.

| $\cos\theta$ bin | North Arm | South Arm |
|---|---|---|
| [-0.6, -0.5] | 0.05 | 0.04 |
| [-0.5, -0.4] | 0.04 | 0.02 |
| [-0.4, -0.3] | 0.02 | 0.02 |
| [-0.3, -0.2] | 0.01 | 0.01 |
| [-0.2, -0.1] | 0.003 | 0.01 |
| [-0.1, 0] | 0.02 | 0.005 |
| [0, 0.1] | 0.02 | 0.004 |
| [0.1, 0.2] | 0.01 | 0.01 |
| [0.2, 0.3] | 0.007 | 0.04 |
| [0.3, 0.4] | 0.007 | 0.005 |
| [0.4, 0.5] | 0.01 | 0.02 |
| [0.5, 0.6] | 0.02 | 0.02 |

effect on the final fit result. The study of data fluctuations with different $\cos\theta$ bin widths on the fitted $\lambda$ value is needed. Figure. 4.28 shows the results from two binning schemes: 20-bin versus 10-bin. Note that a smaller vertical scale is used for this particular set of plots in order to seperate the binning effects for clarity. The data rebin effect is calculated as the absolute value change of the fit function at $\pm 0.6$ as the maximal global systematic error from the binning effect. The error for the north arm is 0.0144 and 0.108 for the south arm. The $\lambda$ values from these two fit functions are given as follows, which are statistically equivalent,

$$\lambda_{20bin} = 0.22 \pm 0.21 \quad \text{(north arm)} \qquad -0.03 \pm 0.16 \quad \text{(south arm)}$$

$$\lambda_{10bin} = 0.18 \pm 0.21 \quad \text{(north arm)} \qquad -0.06 \pm 0.18 \quad \text{(south arm)}$$

where errors are statistical only.

### 4.5.7 Data Bin Shift Effect

The bin shift effect on the fit of the $\cos\theta$ distribution is calculated by choosing a 10-bin binning scheme for two different fit ranges of $\cos\theta$ since no signal is observed when $|\cos\theta| > 0.8$. The results are plotted in Fig. 4.29. The error for the north arm is 0.007 and the same for the south arm.

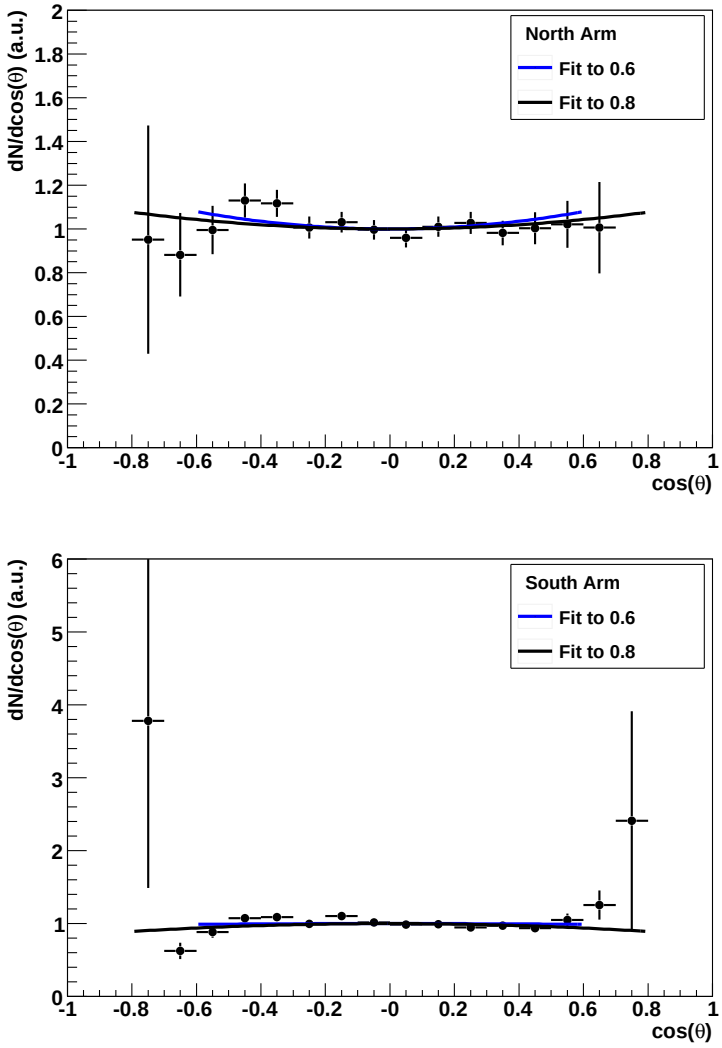


Figure 4.27: (color online) Systematic errors from the fitting edge effect.

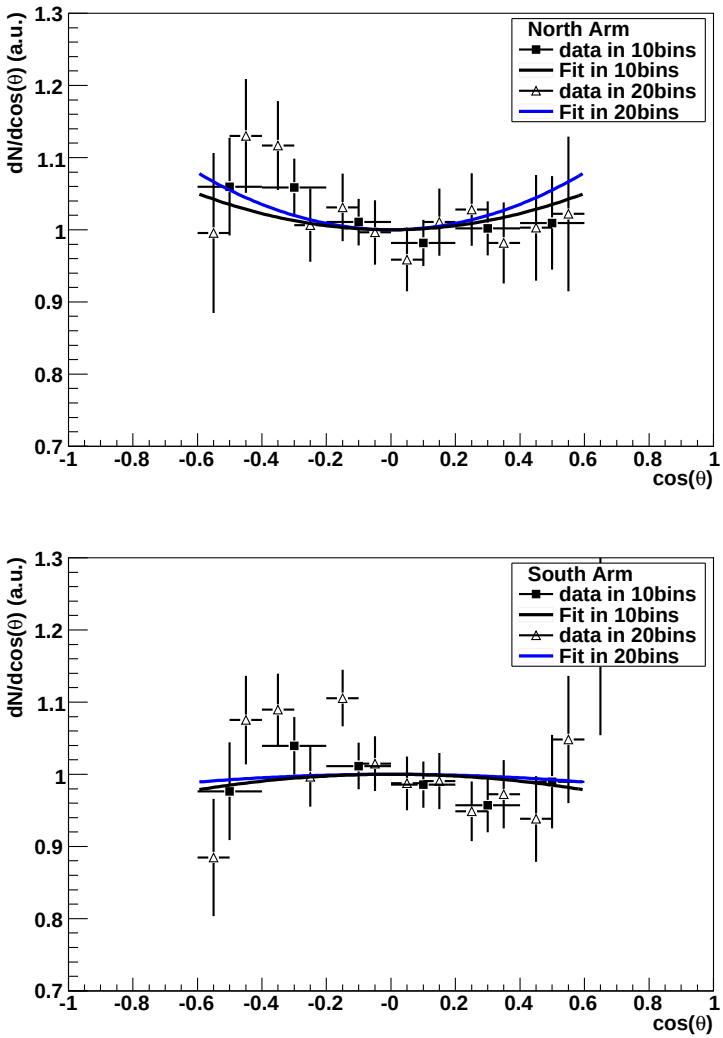


Figure 4.28: (color online) Systematic errors from data rebin effect.

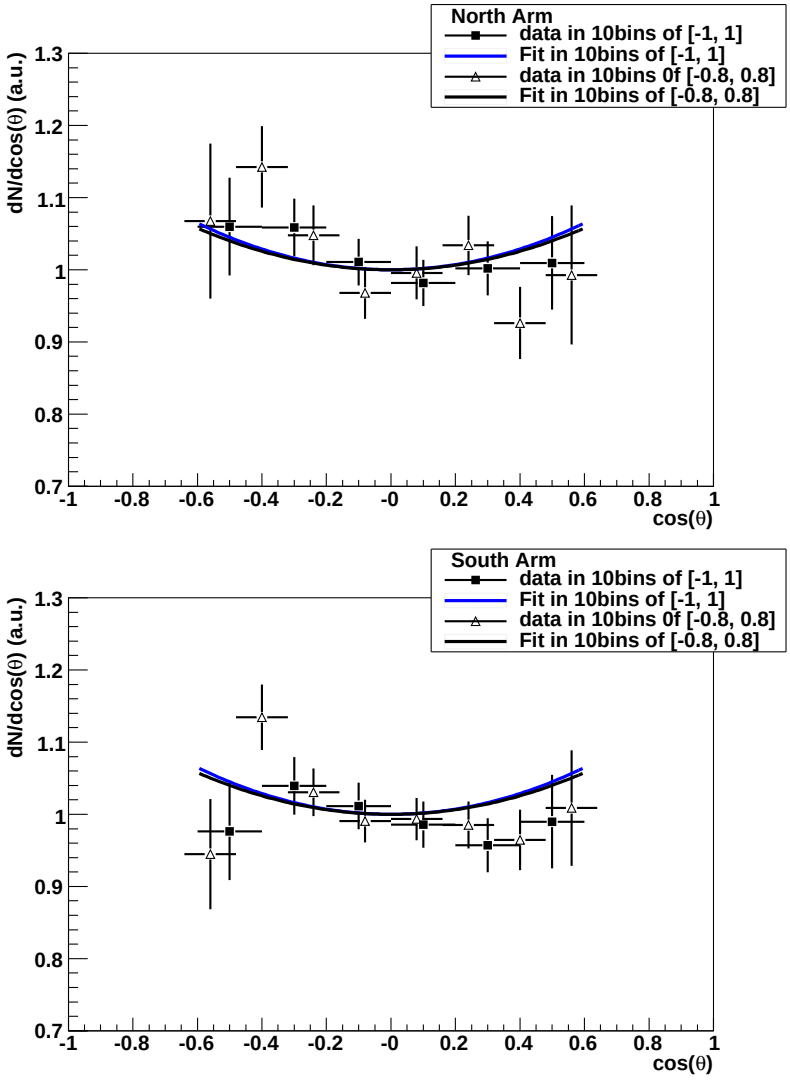


Figure 4.29: (color online) Systematic errors from the bin shift of data.

# Chapter 5

# Results

## 5.1 Polarization Results from Each Muon Arm

The acceptance corrected $\cos\theta$ distributions are fitted with the function $1+\lambda\cos^2\theta$. The final fit results for two (North/South) muon arms are shown in Fig. 5.1. The extracted $J/\psi$ polarization results are tabulated in Table 5.1. The quoted errors are statistical only. To combine the two arm results, the minimum likelihood fit scheme will be used in the next section which combines the statistical and systematic error to optimize the $\lambda$ value.

Table 5.1: The fitted $\lambda$ results of the two arms. The error is statistical only.

| | $\lambda$ parameter |
|---|---|
| North Arm | 0.219±0.207 |
| South Arm | -0.03±0.164 |

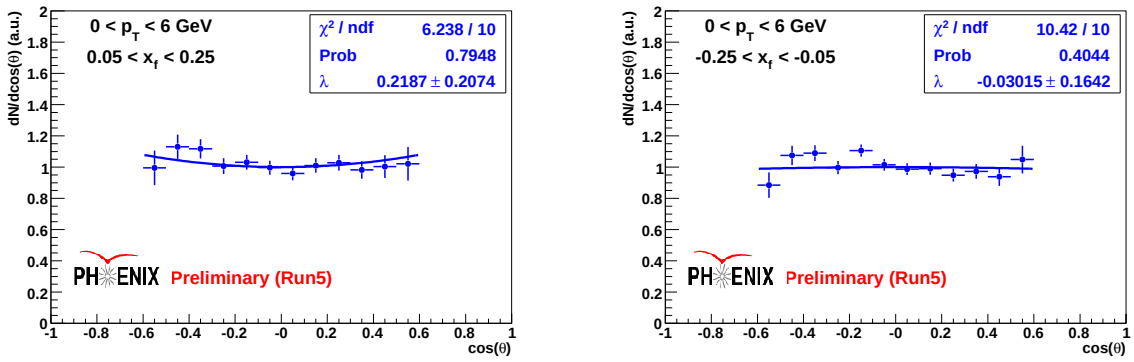


(a) North Arm (b) South Arm

Figure 5.1: Fit results for two muon arms.

## 5.2 Combined Result

The combined $\cos\theta$ distribution is calculated by adding the $\cos\theta$ distribution from each arm weighted by the associated error squared in each $\cos\theta$ bin.

$$(\cos\theta)_{Combined} = (\cos\theta)_N \times \frac{\frac{1}{\sigma_N^2}}{\Sigma\frac{1}{\sigma_i^2}} + (\cos\theta)_S \times \frac{\frac{1}{\sigma_S^2}}{\Sigma\frac{1}{\sigma_i^2}} \tag{5.1}$$

where $i$ = N, S.

The $\lambda$ value is calculated by fitting the combined $\cos\theta$ distribution, with the $1 + \lambda cos^2\theta$ function, with a minimum likelihood method [77, 78]. The likelihood function is defined as:

$$-2\ln L = \sum_{i=1}^{n} \frac{(y_i + \varepsilon_b\sigma_{b_i} + \varepsilon_c y_i\sigma_c - \mu(\overrightarrow{p}))^2}{\sigma_i^2} + \varepsilon_b^2 + \varepsilon_c^2 \tag{5.2}$$

where $y_i$ is each data point in a $\cos\theta$ bin, $\sigma_i$ is the statistical error, $\sigma_{b_i}$ and $\sigma_c$ are the correlated systematic and global systematic errors respectively, and $\varepsilon_b$ and $\varepsilon_c$ are the number of the correlated and global errors being tested. The procedure for applying this method is

briefly described below:

- Add the statistical and systematic errors of each arm separately into the likelihood function. The root macros for this study can be found from the link below

  $http://www.phenix.bnl.gov/viewcvs/offline/analysis/run5pp\_pol\_gsu/Run5pp_Fit/main.C$

  $http://www.phenix.bnl.gov/viewcvs/offline/analysis/run5pp\_pol\_gsu/Run5pp_Fit/data.C$

- Loop lambda between [-0.5, 0.5] with step 0.001
- Loop on $\pm 1$ sigma of systematic errors
- Find $\lambda$ with minimum Likelihood value (corresponding to maxima fit probability).
- Find up and down 0.5 of likelihood value shift as error bar.

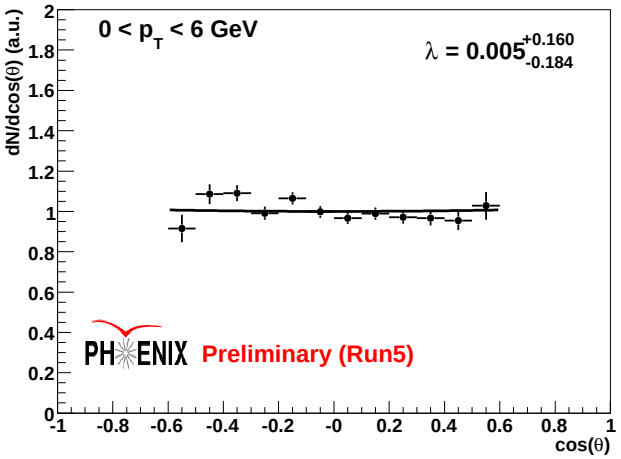


Figure 5.2: Combined fit result of the $J/\psi$ polarization measurement.

The fit result is shown in Fig. 5.2. In conclusion, our measured value of $\lambda$ for $J/\psi$ polarization from Run5 proton+proton collisions is the following:

$$\lambda = 0.005^{+0.160}_{-0.184}$$

where the quoted error is the combined error from systematic and statistical errors. The likelihood fit probability is 97%, which is given in Fig. 5.3.

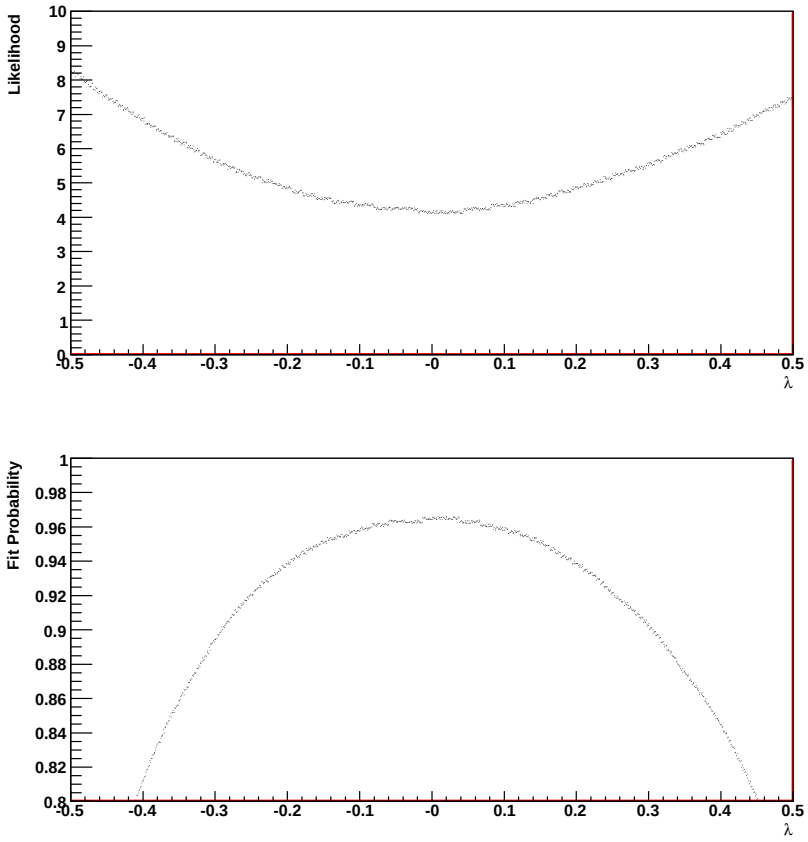


Figure 5.3: The likelihood fit probability distributions. The likelihood value versus $\lambda$ is shown in upper panel. The fit probability versus $\lambda$ is shown in lower panel.

## 5.3 $p_T$ Dependence

An effort to divide the $\cos\theta$ distributions into two $p_T$ bins ($0 < p_T < 1.5$ GeV and $p_T \geq 1.5$ GeV) has been made in order to study the dependence of the $J/\psi$ polarization on $p_T$. The similar studies have been reported by CDF, NA60 and E866 experiments as

discussed in the introduction section. The results are plotted in Fig. 5.4. Given the limited statistics, there will be no quantitative conclusions from this study at the present time.

Table 5.2: The fitted $\lambda$ results of the two arms in two $p_T$ bins. The error is statistical only.

| Arm | $\lambda$ parameter | |
|---|---|---|
| | $0 < p_T < 1.5$ GeV | $p_T \geq 1.5$ GeV |
| North Arm | $0.184 \pm 0.337$ | $0.398 \pm 0.273$ |
| South Arm | $0.184 \pm 0.292$ | $-0.303 \pm 0.186$ |

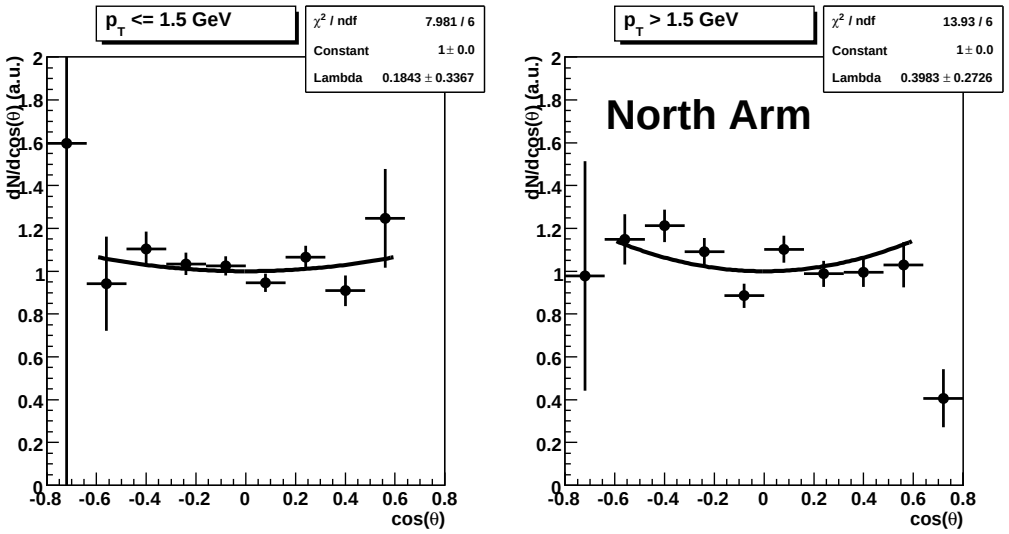


(a) North Arm

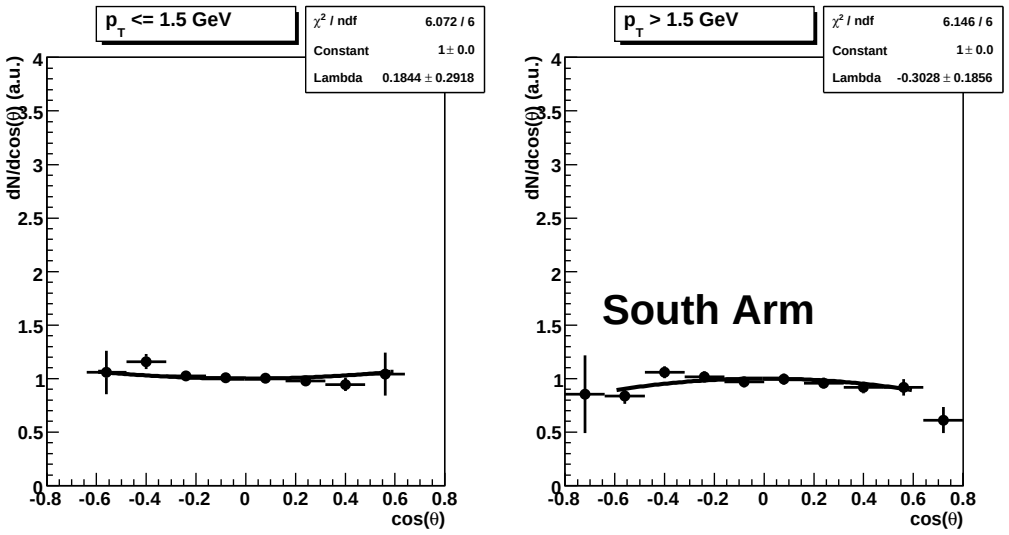


(b) South Arm

Figure 5.4: The $J/\psi$ polarization measurement in two $p_T$ bins.

# Chapter 6

# Conclusions

The angular distributions of decay muons (from $J/\psi$) have been measured with the PHENIX Muon Arms from proton+proton collisions at center mass of energy 200 GeV. The measurement was done in the kinematic coverage of $p_T < 6$ GeV and $|x_f| < 0.25$. No $J/\psi$ polarization has been observed in those regions. At current RHIC energy, the prompt $J/\psi$ (including the direct produced $J/\psi$ from collisions and the feed down from high charmonium states) mainly comes from gluon gluon fusion process. Theoretical models predict no polarization in the relatively low $p_T$ region from this process. The 500 GeV proton+proton collision run at RHIC will help to confirm this measurement and search for the trend in high $p_T$. Furthermore, the large hadron collider (LHC) will shed light on the most critical prediction of $J/\psi$ polarization at large $p_T$.

# Bibliography


[1] David J. Griffiths, *Introduction to Elementary Particles*, John Wiley & Sons, 1987.

[2] Mike Guidry, *Gauge field theories*, John Wiley & Sons, 1991.

[3] Yagi *et al.*, *Quark-Gluon Plasma*, John Wiley & Sons, 1991.

[4] *http://www.bnl.gov/rhic/heavy_ion.htm*

[5] T. Matsui and H. Satz, Phys. Lett. B **178**, 416 (1986).

[6] A. Adare *et al.*, Phys. Rev. Lett. **98**, 232301 (2007).

[7] R. Arnaldi *et al.*, Phys. Rev. Lett. **99**, 132302 (2007).

[8] M. J. Leitch *et al.*, Phys. Rev. Lett. **84**, 3256 (2000).

[9] S. Adler *et al.*, Phys. Rev. Lett. **96**, 012304 (2000).

[10] A. Adare *et al.*, Phys. Rev. C **77**, 024912 (2008).

[11] John C. Collins and Davison E. Soper, Phys. Rev. D **16**, 2219 (1977).

[12] S. Falciano *et al.*, Z. Phys. C **31**, 513 (1986).

[13] T. H. Chang *et al.*, Phys. Rev. Lett. **91**, 211801 (2003).

[14] A. Abulencia *et al.*, Phys. Rev. Lett. **99**, 132001 (2007).

[15] E. Scomparin, J. Phys. G **34**, 463 (2007).

[16] J. J. Aubert *et al.*, Phys. Rev. Lett. **33**, 1404 (1974).

[17] J. E. Augustin *et al.*, Phys. Rev. Lett. **33**, 1406 (1974).

[18] S. W. Herb *et al.*, Phys. Rev. Lett. **39**, 252 (1977).

[19] S. Eidelman *et al.*, Phys. Lett. B **592**, 1 (2004).

[20] Bodwin, Braaten and Lepage, Phys. Rev. D **3**, 1125 (1995).

[21] Bodwin, Braaten and Lepage, Phys. Rev. D **55**, 5853 (1997).

[22] Sean Fleming *et al.*, Phys. Rev. D **64**, 036002 (2001).

[23] Martin Beneke and Michael Kramer, Phys. Rev. D **55**, 5269-5272 (1997).

[24] Peter L. Cho and Mark B. Wise, Phys. Lett. B **346**, 129-136 (1995).

[25] M. B. Einhorn and S. D. Ellis, Phys. Rev. D **12**, 2007 (1975).

[26] T. A. DeGrand and D. Toussaint, Phys. Lett. B **89**, 256 (1980).

[27] J. H.Kuhn *et al.*, Z. Phys. C **5**, 117 (1980).

[28] M. B. Wise, Phys. Lett. B **89**, 229 (1980).

[29] C. H. Chang, Nucl. Phys. B **172**, 425 (1980).

[30] R. Baier and R. Ruckl, Phys. Lett. B **102**, 364 (1981).

[31] E. L. Berger and D. L. Jones, Phys. Rev. D **23**, 1521 (1981).

[32] F. Abe *et al.*, Phys. Rev. Lett. **79**, 572 (1997).

[33] F. Abe *et al.*, Phys. Rev. Lett. **79**, 578 (1997).

[34] H. Haberzettl and J. P. Lansberg, Phys. Rev. Lett. **100**, 032006 (2008).

[35] H. Fritzsch, Phys. Lett. B **67**, 217 (1977).

[36] F. Halzen, Phys. Lett. B **69**, 105 (1977).

[37] N. Brambilla *et al.*, CERN Yellow Report **CERN-2005-005**, (2005).

[38] G. A. Schuler and R. Vogt, Phys. Lett. B **387**, 181 (1996).

[39] J. F. Amundson *et al.*, Phys. Lett. B **390**, 323 (1997).

[40] J. P. Lansberg, Int. J. Mod. Phys. A **21**, 3857 (2006).

[41] Bin Gong and Jian-Xiong Wang, Phys. Rev. Lett. **100**, 232001 (2008).

[42] X.R. Wang, *Ph.D. Thesis* 2002

[43] PHENIX Analysis Note 161

[44] M. Beneke and I. Z. Rothstein, Phys. Lett. B **372**, 157 (1996).

[45] Eric Braaten, Int. J. Mod. Phys. A **12**, 3941 (1997).

[46] M. Beneke, *hep-ph/9712298*

[47] Eric Braaten *et al.*, Phys. Lett. D **62**, 094005 (2000).

[48] Michael Kramer, Nucl. Phys. Proc. Suppl. **93**, 176 (2001).

[49] Michael Kramer, Nucl. Phys. Proc. Suppl. **47**, 141 (2001).

[50] C. Akerlof *et al.*, Phys. Rev. D **48**, 5067 (1993).

[51] A. Gribushin *et al.*, Phys. Rev. D **62**, 012001 (2000).

[52] R. Thomas *et al.*, AIP Conf. Proc. **572**, 1 (2001).

[53] I. Arsene *et al.*, Nucl. Phys. A **757**, 1 (2005).

[54] K. Adcox *et al.*, Nucl. Phys. A **757**, 184 (2005).

[55] B. B. Back *et al.*, Nucl. Phys. A **757**, 28 (2005).

[56] John Adams *et al.*, Nucl. Phys. A **757**, 102 (2005).

[57] PHENIX NIM Articles, *http://www.phenix.bnl.gov/techpapers.html*

[58] PHENIX Inner Detectors, *http://www.phenix.bnl.gov/techpapers.html*

[59] Conceptual Design Report for a Fast Muon Trigger (2007), *(Unpublished)*

[60] PHENIX Muon CDR, *http://www.phenix.bnl.gov/WWW/muon/cdr/cdr.html*

[61] Hiroki Sato, Geophysics and Chemistry **XXXXIV**, (2003).

[62] E. Iarocci *et al.*, Nucl. Instr. and Meth **217**, 30 (1983).

[63] A. Adare *et al.*, Phys. Rev. Lett. **98**, 232002 (2007).

[64] PHENIX Online Systems, *http://www.phenix.bnl.gov/techpapers.html*

[65] J. Newby, *PHENIX Ph.D. Thesis*

[66] Andrew Miles Glenn, *PHENIX Ph.D. Thesis*

[67] E. Mathieson, Nucl. Instr. Meth. A **270**, 602 (1988).

[68] M. L. Brooks and D. M. Lee, Nuclear Science Symposium Conference Record (1996).

[69] Hugo Pereira Da Costa, Note on PHENIX muon offline reconstruction *(Unpublished)*

[70] P. Billoir and S. Qian, Nucl. Instr. Meth. A **295**, 492 (1990).

[71] PHENIX Analysis Note 606

[72] Z. You *et al.*, RIKEN Accel. Prog. Rep. **40**, (2007).

[73] PHENIX Analysis Note 598

[74] *https://www.phenix.bnl.gov/WWW/offline/wikioffline/index.php/Simulations*

[75] PHENIX Analysis Note 406

[76] PHENIX Analysis Note 501

[77] PHENIX Analysis Note 630

[78] PHENIX PPG 079

# Appendix A: Run5 Good Run List

## A.1 North Arm Good Run List

168316 168320 168324 168326 168328 168486 168488 168490 168492 168494 168496
168666 168670 168672 168676 168681 168705 168707 168915 168917 168920 169056 169058
169203 169205 169207 169209 169211 169215 169217 169219 169221 169303 169305 169307
169312 169314 169317 169319 169327 169329 169564 169570 169572 169574 169576 169578
169584 169586 169588 169590 169592 169596 169645 169650 169653 169657 169659 169661
169665 169717 169719 169721 169725 169731 169733 169832 169840 169850 169852 169854
169870 169872 169874 169876 170007 170013 170015 170019 170021 170035 170037 170043
170045 170051 170053 170160 170162 170164 170166 170168 170170 170172 170176 170178
170190 170192 170194 170196 170198 170201 170203 170205 170207 170209 170211 170332
170336 170673 170675 170676 170678 170680 170682 170695 170699 170701 170703 170705
170707 170709 170713 170715 170795 170797 170799 170801 170803 170805 170807 170809
170844 170846 170850 170852 170854 170860 170866 170915 170917 170921 170925 170927
170929 170931 170933 171072 171074 171076 171078 171080 171082 171084 171176 171178
171180 171182 171184 171186 171189 171191 171193 171197 171199 171201 171203 171205
171207 171209 171601 171604 171606 171608 171610 171618 171750 171758 171766 171768

171770 171778 171780 171784 171786 171790 171792 171794 171879 171881 171890 171892
171894 171976 171980 171982 171984 171986 171988 171996 172005 172007 172175 172177
172402 172404 172406 172416 172418 172420 172422 172452 172634 172636 172638 172646
172648 172650 172652 172654 172656 172658 172660 172662 172664 172666 172668 172671
172781 172783 172785 172925 172927 172929 172931 172933 172935 173053 173143 173162
173164 173166 173168 173170 173172 173174 173176 173326 173328 173332 173334 173336
173338 173340 173344 173346 173348 173350 173352 173354 173356 173358 173434 173438
173440 173442 173488 173490 173492 173494 173496 173498 173500 173593 173595 173597
173684 173686 173689 173691 173693 173695 173697 173699 173701 173827 173829 173831
173836 173838 173840 173842 173844 173846 173848 173851 173855 173857 173859 173861
173863 173865 173918 173922 173960 173962 173964 173968 173972 173974 173978 173980
173982 173988 173992 174004 174169 174175 174177 174179 174181 174183 174185 174198
174200 174202 174206 174208 174210 174214 174308 174310 174312 174314 174318 174320
174322 174376 174378 174380 174382 174384 174386 174390 174438 174440 174442 174446
174448 174545 174547 174549 174552 174554 174556 174558 174560 174663 174665 174683
174696 174698 174700 174702 174704 174706 174708 174714 174716 174720 175034 175039
175041 175043 175045 175047 175049 175051 175131 175139 175150 175154 175158 175162
175164 175166 175168 175172 175182 175186 175187 175192 175194 175196 175244 175246
175248 175253 175255 175261 175308 175310 175314 175316 175318 175341 175344 175346
175348 175350 175359 175446 175448 175451 175453 175455 175598 175599 175602 175606
175608 175610 175612 175620 175622 175624 175626 175628 175630 175632 175634 175636
175638 175640 175645 175646 175763 175765 175767 175769 175773 175775 175777 175811

175813 175815 175825 175827 175829 175831 175910 175912 175915 175917 175919 175921
175932 175934 175937 175939 175945 175948 175950 175956 175974 175976 175978 176103
176105 176107 176109 176111 176113 176115 176117 176119 176121 176123 176722 176727
176734 176736 176740 176742 176759 176761 176807 176809 176811 177029 177031 177033
177036 177038 177040 177042 177044 177050 177052 177056 177058 177062 177064 177066
177068 177070 177152 177183 177187 177191 177193 177195 177197 177199 177238 177240
177296 177298 177300 177311 177313 177315 177319 177509 177512 177514 177516 177518
177524 177526 177564 177566 177568 177570 177625 177627 177629 177631 177633 177635
177637 177639 177641 177686 177688 177690 177779 177839 177843 177847 177851 177855
177903 177905 177907 177911 177913 177915 177917 177919 177979 178010 178012 178014
178018 178020 178022 178083 178085 178087 178089 178178 178180 178184 178186 178188
178190 178198 178200 178202 178204 178206 178208 179381 179383 179386 179559 179561
179571 179573 179576 179578 179588 179590 179592 179594 179600 179601 179603 179686
179688 179690 179692 179694 179696 179698 179700 179712 179714 179717 179719 179809
179813 179815 179821 179824 179829 179833 179838 179840 179842 179844 179846

## A.2 South Arm Good Run List

168314 168316 168326 168486 168488 168490 168492 168494 168496 168666 168670
168672 168676 168681 168705 168707 168709 168915 168917 168920 169056 169058 169071
169203 169205 169207 169209 169211 169215 169217 169219 169221 169303 169305 169307
169312 169314 169317 169319 169327 169329 169518 169520 169522 169530 169535 169538
169564 169570 169572 169574 169576 169578 169584 169586 169588 169590 169592 169596

169645 169650 169653 169657 169659 169661 169665 169717 169719 169721 169725 169731

169832 169840 169850 169852 169854 169870 169872 169874 169876 169880 169882 169884

169886 170007 170013 170015 170019 170021 170035 170037 170043 170045 170051 170053

170160 170162 170164 170166 170168 170170 170172 170176 170178 170190 170192 170194

170196 170198 170201 170203 170205 170207 170209 170211 170332 170336 170572 170574

170576 170578 170586 170673 170675 170676 170678 170680 170682 170695 170699 170701

170703 170705 170707 170709 170713 170715 170795 170797 170799 170801 170803 170805

170807 170809 170844 170846 170850 170852 170854 170860 170866 170915 170917 170921

170925 170927 170929 170931 170933 171072 171074 171076 171078 171080 171082 171084

171176 171178 171180 171182 171184 171186 171189 171191 171193 171197 171199 171201

171203 171205 171207 171209 171601 171604 171606 171608 171610 171618 171750 171758

171766 171768 171770 171778 171780 171784 171786 171790 171792 171794 171879 171881

171890 171892 171894 171976 171980 171982 171984 171986 171988 171990 171996 172005

172007 172011 172022 172024 172026 172028 172030 172080 172165 172167 172173 172175

172177 172402 172404 172406 172416 172418 172420 172422 172452 172634 172636 172638

172646 172648 172650 172652 172654 172656 172658 172660 172662 172664 172666 172668

172671 172781 172783 172785 172925 172927 172929 172931 172933 172935 173053 173143

173162 173164 173166 173168 173170 173172 173174 173176 173326 173328 173332 173334

173336 173338 173340 173344 173346 173348 173350 173352 173354 173356 173358 173434

173438 173440 173442 173488 173490 173492 173494 173496 173498 173500 173593 173595

173597 173684 173686 173689 173691 173693 173695 173697 173699 173701 173827 173829

173831 173836 173838 173840 173842 173844 173846 173848 173851 173855 173857 173859

173861 173863 173865 173918 173922 173960 173962 173964 173968 173972 173974 173978

173980 173982 173984 173988 173992 174004 174169 174175 174177 174179 174181 174183

174185 174198 174200 174202 174206 174208 174210 174214 174308 174310 174312 174314

174318 174320 174322 174376 174378 174380 174382 174384 174386 174390 174438 174440

174442 174446 174448 174545 174547 174549 174552 174554 174556 174558 174560 174562

174663 174665 174683 174696 174698 174700 174702 174704 174706 174708 174714 174716

174720 174733 174735 174737 174744 174746 174748 174750 174806 174808 174810 174812

174814 174816 174820 174903 174911 174913 174915 174917 174921 174923 175034 175039

175041 175043 175045 175047 175049 175051 175131 175139 175150 175154 175158 175162

175164 175166 175168 175172 175182 175186 175187 175192 175194 175196 175244 175246

175248 175250 175253 175255 175261 175308 175310 175314 175316 175318 175341 175344

175346 175348 175350 175359 175446 175448 175451 175453 175598 175599 175602 175606

175608 175610 175612 175620 175622 175624 175626 175628 175630 175632 175634 175636

175638 175640 175645 175646 175763 175765 175767 175769 175773 175775 175777 175811

175813 175815 175825 175827 175829 175831 175910 175912 175915 175917 175919 175921

175932 175934 175937 175939 175945 175948 175950 175956 175974 175976 175978 176103

176105 176107 176109 176111 176113 176115 176117 176119 176121 176123 176722 176727

176734 176736 176740 176742 176759 176761 176807 176809 176811 177029 177031 177033

177036 177038 177040 177042 177044 177050 177052 177056 177058 177062 177064 177066

177068 177070 177154 177183 177185 177187 177191 177193 177195 177197 177199 177238

177240 177298 177300 177311 177313 177315 177319 177509 177512 177514 177516 177524

177526 177564 177566 177568 177570 177625 177627 177629 177631 177633 177635 177637

177639 177641 177686 177688 177690 177779 177839 177843 177847 177851 177855 177860
177903 177905 177907 177911 177913 177915 177917 177919 177979 178010 178012 178014
178018 178020 178022 178083 178085 178087 178089 178178 178180 178184 178186 178188
178190 178198 178200 178202 178204 178206 178208 178422 178424 178428 178430 178527
178529 178531 178543 178545 178547 178549 178551 178553 178555 178565 178567 178569
178571 178573 178575 178577 178579 178581 178585 178600 178604 178606 178745 178748
178750 178752 178754 178756 178759 178804 178806 178808 178810 178812 178814 178818
178820 178823 178825 178911 178913 178918 178920 178922 178928 178932 178934 178938
178940 178942 178944 178946 178948 178986 178988 178990 178995 178997 178999 179006
179008 179013 179064 179066 179068 179070 179072 179074 179076 179078 179080 179092
179094 179098 179100 179102 179104 179145 179147 179152 179155 179157 179159 179161
179163 179165 179167 179169 179216 179218 179220 179222 179224 179226 179228 179310
179315 179317 179319 179321 179323 179328 179377 179383 179386 179559 179561 179571
179573 179576 179578 179580 179588 179590 179592 179594 179600 179601 179603 179686
179690 179698 179700 179712 179717 179719 179809 179813 179821 179824 179829 179833
179838 179840 179846

# Appendix B: Helicity Frame Lorentz Transformation

## B.1 Introduction

In order to calculate the angular distribution in the helicity frame, we need to make Lorentz transformation of the $J/\psi$ four momentum between the collision center of mass (CM) frame and the $J/\psi$ rest frame. The detailed transformation is given below. The Lorentz transformation between various frames is defined as: [12]

$$E^* = \gamma(E - \overrightarrow{\beta} * \overrightarrow{P}) \tag{B.1.1}$$

$$\overrightarrow{P}^* = \overrightarrow{P} + \frac{\gamma - 1}{\beta^2}(\overrightarrow{\beta} * \overrightarrow{P}) - \gamma \overrightarrow{\beta} E \tag{B.1.2}$$

Here we use * to denote coordinates in the $J/\psi$ helicity frame and no superscript for the CM frame. In this case, $\gamma = E_\gamma / M_\gamma$ and $\beta = \frac{\sqrt{{P_T}^2 + {P_L}^2}}{E_\gamma}$, in which the subscript $\gamma$ is referred to as $J/\psi$ and the $\gamma$ is referred to as Lorentz factor.

## B.2 Lorentz Transformation to Helicity Frame

Here we derive the Lorentz transformation of the muon four momentum from the CM frame to the $J/\psi$ helicity frame. In Cartesian coordinates, the transformation of the

muon four momentum is:

$$E_\mu{}^* = \frac{1}{M_\gamma}(E_\mu E_\gamma - P_\mu P_\gamma cos\alpha) \tag{B.2.3}$$

$$P_{\mu x}{}^* = P_{\mu x} + (\frac{E_\gamma}{M_\gamma} - 1)\frac{P_\mu P_{\gamma x} cos\alpha}{P_\gamma} - \frac{E_\mu P_{\gamma x}}{M_\gamma} \tag{B.2.4}$$

$$P_{\mu y}{}^* = P_{\mu y} + (\frac{E_\gamma}{M_\gamma} - 1)\frac{P_\mu P_{\gamma y} cos\alpha}{P_\gamma} - \frac{E_\mu P_{\gamma y}}{M_\gamma} \tag{B.2.5}$$

$$P_{\mu z}{}^* = P_{\mu z} + (\frac{E_\gamma}{M_\gamma} - 1)\frac{P_\mu P_{\gamma z} cos\alpha}{P_\gamma} - \frac{E_\mu P_{\gamma z}}{M_\gamma} \tag{B.2.6}$$

Here, ( $E_\mu$, $\overrightarrow{P}_\mu$ ) is the muon four-momentum in the CM frame, ($E_\gamma$, $\overrightarrow{P}_\gamma$) is the $J/\psi$ four momentum in the CM frame, and $\alpha$ is the angle between one of the muon momenta with the $J/\psi$ momentum direction.

Now we need to rotate the coordinates to align the $z$ axis with the $J/\psi$ momentum direction. We first rotate the $x$ and $y$ axis about the $z$-axis through the angle $\phi_\gamma$ ($cos\phi_\gamma = \frac{P_{\gamma x}}{\sqrt{{P_{\gamma x}}^2 + {P_{\gamma y}}^2}}$)

$$\begin{pmatrix} P_{\mu x}{}^* \\ P_{\mu y}{}^* \end{pmatrix} = \begin{pmatrix} cos\phi_\gamma & sin\phi_\gamma \\ -sin\phi_\gamma & cos\phi_\gamma \end{pmatrix} \begin{pmatrix} P_{\mu x} + (\frac{E_\gamma}{M_\gamma} - 1)\frac{P_\mu P_{\gamma x} cos\alpha}{P_\gamma} - \frac{E_\mu P_{\gamma x}}{M_\gamma} \\ P_{\mu y} + (\frac{E_\gamma}{M_\gamma} - 1)\frac{P_\mu P_{\gamma y} cos\alpha}{P_\gamma} - \frac{E_\mu P_{\gamma y}}{M_\gamma} \end{pmatrix} \tag{B.2.7}$$

here $\frac{P_{\mu x}}{P_\mu} = cos\phi_\mu$, $\frac{P_{\mu y}}{P_\mu} = sin\phi_\mu$, $\frac{P_{\gamma x}}{P_\gamma} = cos\phi_\gamma$, $\frac{P_{\gamma y}}{P_\gamma} = sin\phi_\gamma$.

$$Eq.\ (B.2.7) = \begin{pmatrix} P_\mu cos(\phi_\mu - \phi_\gamma) + (\frac{E_\gamma}{M_\gamma} - 1)P_\mu cos\alpha - \frac{E_\mu}{M_\gamma}P_\gamma \\ P_\mu sin(\phi_\mu + \phi_\gamma) \end{pmatrix} \tag{B.2.8}$$

Then we rotate the $x$ and $z$ axis about the $y$-axis through the angle $\theta_\gamma$ ($cos\theta_\gamma = \frac{P_{\gamma z}}{P_\gamma}$)

$$\begin{pmatrix} P_{\mu x}{}^* \\ P_{\mu z}{}^* \end{pmatrix} = \begin{pmatrix} cos\theta_\gamma & -sin\theta_\gamma \\ sin\theta_\gamma & cos\theta_\gamma \end{pmatrix} \begin{pmatrix} P_\mu cos(\phi_\mu - \phi_\gamma) + (\frac{E_\gamma}{M_\gamma} - 1)P_\mu cos\alpha - \frac{E_\mu}{M_\gamma}P_\gamma \\ P_{\mu z} + (\frac{E_\gamma}{M_\gamma} - 1)\frac{P_\mu P_{\gamma z} cos\alpha}{P_\gamma} - \frac{E_\mu P_{\gamma z}}{M_\gamma} \end{pmatrix}$$

$$= \begin{pmatrix} P_\mu cos\theta_\gamma cos(\phi_\mu - \phi_\gamma) + [(\frac{E_\gamma}{M_\gamma} - 1)P_\mu cos\alpha - \frac{E_\mu}{M_\gamma}P_\gamma](cos\theta_\gamma - \frac{1}{2}sin2\theta_\gamma) - sin\theta_\gamma P_{\mu z} \\ P_\mu sin\theta_\gamma cos(\phi_\mu - \phi_\gamma) + [(\frac{E_\gamma}{M_\gamma} - 1)P_\mu cos\alpha - \frac{E_\mu}{M_\gamma}P_\gamma](sin\theta_\gamma + {cos\theta_\gamma}^2) + cos\theta_\gamma P_{\mu z} \end{pmatrix}$$

Finally we get the transformed muon momentum in the $J/\psi$ helicity frame:

$$\begin{pmatrix} {E_\mu}^* \\ {P_{\mu x}}^* \\ {P_{\mu y}}^* \\ {P_{\mu z}}^* \end{pmatrix} = \begin{pmatrix} \frac{1}{M_\gamma}(E_\mu E_\gamma - P_\mu P_\gamma cos\alpha) \\ P_\mu cos\theta_\gamma cos(\phi_\mu - \phi_\gamma) + [(\frac{E_\gamma}{M_\gamma} - 1)P_\mu cos\alpha - \frac{E_\mu}{M_\gamma}P_\gamma](cos\theta_\gamma - \frac{1}{2}sin2\theta_\gamma) - sin\theta_\gamma P_{\mu z} \\ P_\mu sin(\phi_\mu + \phi_\gamma) \\ P_\mu sin\theta_\gamma cos(\phi_\mu - \phi_\gamma) + [(\frac{E_\gamma}{M_\gamma} - 1)P_\mu cos\alpha - \frac{E_\mu}{M_\gamma}P_\gamma](sin\theta_\gamma + {cos\theta_\gamma}^2) + cos\theta_\gamma P_{\mu z} \end{pmatrix} \tag{B.2.9}$$

## B.3 Lorentz Transformation to CM Frame

Here we derive the Lorentz transformation of the muon four momentum from the $J/\psi$ helicity frame back to the CM frame. The muon four momentum in the $J/\psi$ helicity frame is defined as:

$${E_{\mu 1}}^* = {E_{\mu 2}}^* = M_\gamma/2 = {E_\mu}^* \tag{B.3.10}$$

$${P_{\mu 1}}^* = {P_{\mu 2}}^* = \sqrt{{{E_{\mu 1}}^*}^2 - {m_\mu}^2} = \sqrt{\frac{{M_\gamma}^2}{4} - {m_\mu}^2} = {P_\mu}^* \tag{B.3.11}$$

$${P_{\mu 1T}}^* = -{P_{\mu 2T}}^* = {P_\mu}^* sin{\theta_\mu}^* \tag{B.3.12}$$

$${P_{\mu 1x}}^* = -{P_{\mu 2x}}^* = {P_\mu}^* sin{\theta_\mu}^* cos{\phi_\mu}^* \tag{B.3.13}$$

$${P_{\mu 1y}}^* = -{P_{\mu 2y}}^* = {P_\mu}^* sin{\theta_\mu}^* sin{\phi_\mu}^* \tag{B.3.14}$$

$${P_{\mu 1z}}^* = -{P_{\mu 2z}}^* = {P_\mu}^* cos{\theta_\mu}^* \tag{B.3.15}$$

where $\theta_\mu^* \epsilon [0, \pi]$ and $\phi_\mu^* \epsilon [0, 2\pi]$.

Before performing the Lorentz transformation, we need to first recover the $z$ axis of Cartesian coordinate from the $J/\psi$ momentum direction to it's original direction. So we first rotate the $x^*$ and $z^*$ axis about the $y^*$ through the angle $(-\theta_\gamma)$

$$\begin{pmatrix} cos\theta_\gamma & sin\theta_\gamma \\ -sin\theta_\gamma & cos\theta_\gamma \end{pmatrix} \begin{pmatrix} {P_{\mu x}}^* \\ {P_{\mu z}}^* \end{pmatrix} = \begin{pmatrix} {P_{\mu x}}^* cos\theta_\gamma + {P_{\mu z}}^* sin\theta_\gamma \\ -{P_{\mu x}}^* sin\theta_\gamma + {P_{\mu z}}^* cos\theta_\gamma \end{pmatrix} \tag{B.3.16}$$

Then we rotate the $x^*$ and $y^*$ axis about the $z^*$ through the angle $(-\phi_\gamma)$

$$\begin{pmatrix} cos\phi_\gamma & -sin\phi_\gamma \\ sin\phi_\gamma & cos\phi_\gamma \end{pmatrix} \begin{pmatrix} {P_{\mu x}}^* cos\theta_\gamma + {P_{\mu z}}^* sin\theta_\gamma \\ {P_{\mu y}}^* \end{pmatrix} \tag{B.3.17}$$

$$= \begin{pmatrix} {P_{\mu x}}^* cos\theta_\gamma cos\phi_\gamma + {P_{\mu z}}^* sin\theta_\gamma cos\phi_\gamma - {P_{\mu y}}^* sin\phi_\gamma \\ {P_{\mu x}}^* cos\theta\gamma sin\phi_\gamma + {P_{\mu z}}^* sin\theta_\gamma sin\phi_\gamma + {P_{\mu y}}^* cos\phi_\gamma \end{pmatrix} \tag{B.3.18}$$

The four momentum of the muon after the rotation is given as:

$$\begin{pmatrix} {P_{\mu x}}^{*'} \\ {P_{\mu y}}^{*'} \\ {P_{\mu z}}^{*'} \end{pmatrix} = \begin{pmatrix} {P_{\mu x}}^* cos\theta_\gamma cos\phi_\gamma - {P_{\mu y}}^* sin\phi_\gamma + {P_{\mu z}}^* sin\theta_\gamma cos\phi_\gamma \\ {P_{\mu x}}^* cos\theta\gamma sin\phi_\gamma + {P_{\mu y}}^* cos\phi_\gamma + {P_{\mu z}}^* sin\theta_\gamma sin\phi_\gamma \\ -{P_{\mu x}}^* sin\theta_\gamma + {P_{\mu z}}^* cos\theta_\gamma \end{pmatrix} \tag{B.3.19}$$

Similar to B.1.1 and B.1.2, the inverse Lorentz transformation formula (from the $J/\psi$ helicity frame to the CM frame) is:

$$E_\mu = \gamma(E_\mu{}^{*'} + \overrightarrow{\beta} * \overrightarrow{P_\mu}^{*'}) \tag{B.3.20}$$

$$\overrightarrow{P}_\mu = \overrightarrow{P_\mu}^{*'} + \frac{\gamma - 1}{\beta^2}(\overrightarrow{\beta} * \overrightarrow{P_\mu}^{*'})\overrightarrow{\beta} + \gamma \overrightarrow{\beta} E_\mu{}^{*'} \tag{B.3.21}$$

Here, $\gamma = E_\gamma / M_\gamma$ and $\beta = (\frac{P_{\gamma T} cos\phi_\gamma}{E_\gamma}, \frac{P_{\gamma T} SIN\phi_\gamma}{E_\gamma}, \frac{P_{\gamma L}}{E_\gamma})$. So the Lorentz transformation for $E_\mu$ is,

$$E_\mu = \frac{E_\mu{}^{*'} E_\gamma}{M_\gamma} + \frac{P_\mu{}^{*'} P_\gamma}{M_\gamma}[cos\theta_\gamma cos\theta_\mu{}^* + sin\theta_\gamma sin\theta_\mu{}^* cos(\phi_\gamma - \phi_\mu{}^*)] \tag{B.3.22}$$

if we define $cos\alpha = cos\theta_\gamma cos\theta_\mu{}^* + sin\theta_\gamma sin\theta_\mu{}^* cos(\phi_\gamma - \phi_\mu{}^*)$, the four momentum transfor-

mation is given as:

$$\begin{pmatrix} E_\mu \\ P_{\mu x} \\ P_{\mu y} \\ P_{\mu z} \end{pmatrix} = \begin{pmatrix} \frac{{E_\mu}^{*'} E_\gamma}{M_\gamma} + \frac{{P_\mu}^{*'} P_\gamma}{M_\gamma} cos\alpha \\ {P_{\mu x}}^{*'} + P_{\gamma x}[(\frac{E_\gamma}{M_\gamma} - 1)\frac{{P_\mu}^{*'} cos\alpha}{P_\gamma} + \frac{{E_\mu}^{*'}}{M_\gamma}] \\ {P_{\mu y}}^{*'} + P_{\gamma y}[(\frac{E_\gamma}{M_\gamma} - 1)\frac{{P_\mu}^{*'} cos\alpha}{P_\gamma} + \frac{{E_\mu}^{*'}}{M_\gamma}] \\ {P_{\mu z}}^{*'} + P_{\gamma x}[(\frac{E_\gamma}{M_\gamma} - 1)\frac{{P_\mu}^{*'} cos\alpha}{P_\gamma} + \frac{{E_\mu}^{*'}}{M_\gamma}] \end{pmatrix} \tag{B.3.23}$$

# Appendix C: List of Variables

- $\sqrt{s}$: Center-of-mass energy of the collision system.
- $p_T$ : Transverse momentum.
- $x_f$ : Longitudinal momentum fraction of a particle. It is defined as the pair longitudinal momentum $P_L$ divided by its maximum kinematically allowed value $P_{L,max}$ in the collision center-of-mass frame. It relates to the Bjorken x, the fraction of the hadron momentum carried by a parton in the hadron boosted to the infinite-momentum frame, of the beam parton $x_1$ and of the target parton $x_2$ by $x_f = (1 - m^2/S) = x_1 - x_2$.
- $y$ : Rapidity. It is defined as $y = \frac{1}{2}\ln(\frac{E+P_z}{E-P_z})$, where $E$ is the energy and $P_z$ is the longitudinal momentum of the particle.
- $\eta$ : Pseudorapidity. It is defined as $\eta = -\ln[tan(\frac{\theta}{2})]$, where $\theta$ is the angle between the particle momentum $\overrightarrow{p}$ and the $z$ axis.
- $\theta$ : Polar angle.
- $\phi$ : Azimuthal angle.